

**The *IRIS* Far-Infrared Galaxy Survey :
Expected Number Count, Redshift, and Perspective**

**TSUTOMU T. TAKEUCHI^{1,2}, HIROYUKI HIRASHITA^{1,2}, KOUJI OHTA¹,
TAKASHI G. HATTORI¹, TAKAKO T. ISHII^{1,3},**

¹ Department of Astronomy, Faculty of Science, Kyoto University, Sakyo-ku, Kyoto
606-8502, JAPAN

² Research Fellow of the Japan Society for the Promotion of Science

³ Kwasan and Hida Observatories, Yamashina-ku, Kyoto University, Kyoto,
607-8471, JAPAN

Electronic mail: takeuchi, hirasita, ohta, hattori, ishii@kusastro.kyoto-u.ac.jp

AND

HIROSHI SHIBAI⁴

⁴ Division of Particle and Astrophysical Sciences, School of Science, Nagoya University,
Chikusa-ku, Nagoya, 464-8602, JAPAN

Electronic mail: shibai@toyo.phys.nagoya-u.ac.jp

ABSTRACT

Infrared Imaging Surveyor (*IRIS*) is a satellite which will be launched in the beginning of 2003. One of the main purposes of the *IRIS* mission is an all-sky survey at far-infrared (FIR) with a flux limit much deeper than that of *IRAS*. In order to examine the performance of the survey, we estimated the FIR galaxy counts in four (50, 70, 120, and 150 μm) bands based on some models. We adopted a multicomponent model which consists of cirrus and starburst components for galaxy spectra, and the nearby FIR luminosity function derived from that of *IRAS* galaxies. We derived the number counts, redshift distributions, and infrared diffuse background radiation spectra for i) no evolution, ii) pure luminosity evolution, iii) pure density evolution with $q_0 = 0.1$ and 0.5. We found that a large number of galaxies (\sim a few $\times 10^6$ in the whole sky) will be detected in this survey. With the aid of a vast number of detection, we will detect the effect of galaxy evolution, and evaluate the amplitude of evolution at least in the nearby universe in the *IRIS* survey, though it will be still difficult to constrain which type of evolution takes place from the number count alone. We also studied the estimation of redshifts of detected galaxies by their infrared colors alone. Although significant contamination takes place

among nearby faint galaxies and high- z ones, we found that rough estimation of galaxy redshift can be practicable by jointly using present and future optical surveys.

Subject headings: galaxies: evolution — galaxies: formation — galaxies: starburst — infrared radiation

1. INTRODUCTION

One of the important problems in astrophysics is to trace back the galaxy evolution to the epoch at which galaxies formed. Recently Steidel and collaborators have pioneered and widely utilized a multicolor technique to select young galaxies by use of Lyman-break dropout, and discovered a class of actively star-forming galaxies in high-redshift ($z \gtrsim 3$) Universe (Steidel, Pettini, & Hamilton 1995; Steidel et al. 1996; Lowenthal et al. 1997). Some lens-magnified normal galaxies at high redshift also show rather high star formation rate (Ebbels et al. 1996; Yee et al. 1996; Franx et al. 1997; Trager et al. 1997). Furthermore, Ohta et al. (1996) and Omont et al. (1996) detected CO emission lines in the quasar BR1202–0725 at redshift $z = 4.69$, suggesting the existence of a large amount of molecular gas and dust in the object. All of these results imply that strong star formation and synthesis of heavy elements have already occurred in such an early stage of the Universe. The violent initial bursts of star formation must have produced large amount of dust, so that the optical deep surveys of protogalaxies inevitably suffer from the bias induced by severe dust extinction. The dust particles reprocess the starlight, and bulk of the bolometric luminosity of these young galaxies will be emitted at far-infrared (FIR) – submillimeter (sub-mm) wavelengths.

The FIR emission from galaxies, especially from those are so faint that we are unable to resolve, produces the cosmic infrared background radiation (CIRB). Therefore the CIRB provides important information on the past star formation history of galaxies including the inaccessible sources (e.g. Bond, Carr, & Hogan 1986; Burigana et al. 1997). The recently reported detection of an isotropic diffuse light at $\lambda \sim 100 - 200 \mu\text{m}$ has given this field new impetus (Puget et al. 1996; see also Fixsen et al. 1998; Hauser et al. 1998).

Meanwhile, galaxy evolution at low redshift ($z \lesssim 1$) has also crucial implications to cosmological studies. Lilly et al. (1996) found the rapid rise of the comoving luminosity density with redshift in ultraviolet (UV), optical, and near-IR wavelengths up to $z \sim 1$. Madau et al. (1996) interpreted this as an increase of comoving star formation rate (SFR) by a factor of ten in the redshift interval $z = 0 - 1$. Subsequent observational evidences

support this conclusion (e.g. Ellis et al. 1996; Tresse & Maddox 1998). Because FIR is the wavelength at which dust reradiates the optical – UV radiation from young stars, the steeply increasing SFR density is expected to propose a significant increment of FIR source counts, which may be related to the evolving population of star-forming galaxies discovered by *Infrared Astronomical Satellite (IRAS)* (Hacking & Houck 1987 (HH87); Hacking, Condon, & Houck 1987; Saunders et al. 1990; Oliver, Rowan-Robinson, & Saunders 1992; Ashby et al. 1996).

For the understanding of FIR properties of actively star-forming galaxies, vast advances have been provided by the *IRAS* all-sky survey with a flux limit of ~ 1 Jy at $60 \mu\text{m}$ (for a review, Soifer, Houck, & Neugebauer 1987a). Recently quite important results have been reported from the *Infrared Space Observatory (ISO)* (Kessler et al. 1996). Kawara et al. 1998 (K98) have performed a deep survey at the Lockman Hole region with a flux limit of 45 mJy at $175 \mu\text{m}$. They reported that the surface density of the sources brighter than 150 mJy at $175 \mu\text{m}$ approximately reproduced by the model of Guiderdoni et al. (1997). Although this survey is much deeper than the *IRAS* survey, it covers only a small solid angle of the sky (1600 arcmin^2) and much wider sky coverage is necessary in the next step to obtain a huge sample.

Infrared Imaging Surveyor (*IRIS*¹) is a next generation infrared satellite, which will be launched in the beginning of 2003. A near-/mid-infrared camera (IRC) and a FIR scanner (FIS) are planned to be on-board. One of the main purposes of the *IRIS* mission is a FIR all-sky survey deeper than *IRAS* surveys, and the FIR instrument represents a significant improvement over *IRAS*, so that much higher sensitivity is achieved (detection limit is ~ 20 mJy at $50 \mu\text{m}$, ~ 30 mJy at $120 \mu\text{m}$, and ~ 50 mJy at $150 \mu\text{m}$).

In order to examine the performance of the survey, we estimated the FIR galaxy counts based on a simple model with various sets of cosmological parameters and evolution types. There have been a number of attempts to predict the source counts or the CIRB properties. The models of the source counts and CIRB generally fall into two categories (e.g. Eales & Edmunds 1997): one is tied closely to the nearby observational results but makes no attempts to incorporate detailed galaxy evolution models (e.g. Beichman & Helou 1991 (BH91); Pearson & Rowan-Robinson 1996). These models are based on the local FIR luminosity function (LF) and the observational evidence of spectral energy distribution (SED) of galaxies in the FIR – sub-mm, with the assumptions of simple functional forms for the evolution. The other is based on the models constructed by detailed physical processes related to the evolution of galaxies (e.g. Franceschini et al. 1994; Guiderdoni et

¹The project name of *IRIS* is Astro-F.

al. 1997). They tend to be very complex with large numbers of parameters, which give rise to a number of related problems poorly understood. Ellis (1997) names the former “empirical approach” and the latter “*ab initio* approach”. Despite each category of models has its own merits and demerits, we preferred the “empirical approach”, because it is free of the parameters which are inherent in specific models and thus easy to understand the dependence on the cosmological and evolutionary parameters.

This paper is organized as follows. In section 2, we describe the general formulation of our model. The parameters to execute our calculations and their consistency with previous survey results are examined in section 3. We present the *IRIS*-based results and related discussions in section 4, and our conclusions are summarized in section 5.

2. MODEL DESCRIPTION

2.1. Spectral Energy Distribution of Galaxies

First we construct a model of galaxy SED from FIR to sub-mm wavelengths. The FIR emission originates from several dust components of different grain sizes and temperatures, reprocessing the interstellar radiation (Désert, Boulanger, & Puget 1990). Rowan-Robinson & Crawford (1989)(RC89) showed that the FIR spectrum of *IRAS* galaxies is well fitted by the combination of two components: cool disk emission from interstellar dust (cirrus component) and hot starburst-induced emission, from optically thick dust clouds heated by numbers of OB stars. Therefore we consider a simple model of two components, cool cirrus and hot starbursts as the components of our model SEDs of galaxies. We must note that we ignore the power-law component seen in AGN or QSO spectra, because contribution of these power-law objects is expected to be negligible in number compared with the total number of infrared (IR) sources, and because their luminosity contribution is also small in FIR wavelength range, though it might be slightly higher in very high- z Universe (Pearson 1996).

We define the total IR luminosity L_{IR} as follows:

$$L_{\text{IR}} = \int_{\nu_{\text{min}}}^{\nu_{\text{max}}} L(\nu) d\nu, \quad (1)$$

where $L(\nu)$ is the monochromatic luminosity of a galaxy, and we put $\nu_{\text{min}} = 3 \times 10^{11}$ Hz ($\lambda_{\text{max}} = 1$ mm) and $\nu_{\text{max}} = 10^{14}$ Hz ($\lambda_{\text{min}} = 3 \mu\text{m}$).

Here we assume that the IR luminosity of a galaxy less than $10^{10}L_{\odot}$ is composed of the cirrus component $L_c(\nu)$ only. For galaxies with $L_{\text{IR}} > 10^{10}L_{\odot}$, the IR luminosity in excess

of $10^{10} L_{\odot}$ (i.e., $L_{\text{IR}} - 10^{10} L_{\odot}$), is assumed to come from the starburst component, denoted as $L_s(\nu)$. Thus, the composite SED of a galaxy is expressed as follows;

$$L(\nu) = \begin{cases} L_c(\nu) & \text{for } L_{\text{IR}} < 10^{10} L_{\odot}; \\ L_c(\nu) + L_s(\nu) & \text{for } L_{\text{IR}} > 10^{10} L_{\odot}, \end{cases} \quad (2)$$

where $L_c(\nu)$ and $L_s(\nu)$ are normalized as

$$L_c \equiv \int_{\nu_{\text{min}}}^{\nu_{\text{max}}} L_c(\nu) d\nu = \begin{cases} L_{\text{IR}} & \text{for } L_{\text{IR}} < 10^{10} L_{\odot}; \\ 10^{10} L_{\odot} & \text{for } L_{\text{IR}} > 10^{10} L_{\odot}, \end{cases} \quad (3)$$

and

$$L_s \equiv \int_{\nu_{\text{min}}}^{\nu_{\text{max}}} L_s(\nu) d\nu = \begin{cases} 0 & \text{for } L_{\text{IR}} < 10^{10} L_{\odot}; \\ L_{\text{IR}} - 10^{10} L_{\odot} & \text{for } L_{\text{IR}} > 10^{10} L_{\odot}. \end{cases} \quad (4)$$

This model formulation is in line of BH91. So as to make our model work well, L_{IR} should be uniquely defined from the value $L(\nu)$ at any frequency ν . The SEDs depend only on L_{IR} , and do not vary with redshift as long as L_{IR} of a galaxy is constant.

2.1.1. The cirrus component

The cirrus spectrum we used is based on the model of Désert et al. (1990). Their model spectrum is the sum of three subcomponents, that are polycyclic aromatic hydrocarbons (PAHs; peaked at $\sim 10 \mu\text{m}$), very small grains (peaked at $\sim 60 \mu\text{m}$), and big grains (peaked at $\sim 100 \mu\text{m}$). No IR emission lines are included in our model. As mentioned above, galaxies with $L_{\text{IR}} < 10^{10} L_{\odot}$ only have the cirrus component in the present model. At each IR luminosity, the galaxy SED is scaled properly to yield the given L_{IR} according to eq.(3).

2.1.2. The Starburst Component

As for galaxies with $L_{\text{IR}} \gtrsim 10^{10-11} L_{\odot}$, bulk of the IR luminosity is due to dust emission from an intense starburst in giant molecular clouds (e.g. Sanders & Mirabel 1996). Therefore we assume that, for galaxies whose IR luminosities are brighter than $10^{10} L_{\odot}$, their IR luminosities in excess of $10^{10} L_{\odot}$ consist of starbursts with two different temperatures according to BH91. We give the starburst flux $L_s(\nu)$ as a superposition of thermal blackbody radiation spectrum of temperature T_{hot} (we call it “hot component” of starbursts) and that of T_{cool} (“cool component”), multiplied with dust emissivity. We

adopted the wavelength-dependent dust emissivity $\propto \lambda^{-1} \propto \nu$ (RC89). By using the above temperatures, $L_s(\nu)$ is expressed by

$$L_s(\nu) = \alpha \nu B_\nu(T_{\text{cool}}) + \beta \nu B_\nu(T_{\text{hot}}), \quad (5)$$

where $B_\nu(T)$ is the Planck function with temperature T and both α and β are normalizing constants (RC89). The temperatures of the starburst components are given by

$$T_{\text{cool}} = 60 \left(\frac{L_s}{10^{11} L_\odot} \right)^{0.1} \text{ K}, \quad (6)$$

and

$$T_{\text{hot}} = 175 \left(\frac{L_s}{10^{11} L_\odot} \right)^{0.1} \text{ K} \quad (7)$$

(BH91; see also Rieke & Lebofsky 1986; Helou 1986; Soifer et al. 1987b). The cool component gives a good representation of the larger (0.01–0.1 μm) grains modeled by Rowan-Robinson (1986), and the hot component gives an approximate representation of the very small grains postulated by Boulanger, Baud, & van Albada (1985), Draine & Anderson (1985), and Rowan-Robinson (1992).

Normalizing constants, α and β , are determined by the following equations (BH91):

$$0.7L_s = \alpha \int_{\nu_{\text{min}}}^{\nu_{\text{max}}} \nu B_\nu(T_{\text{cool}}) d\nu, \quad (8)$$

$$0.3L_s = \beta \int_{\nu_{\text{min}}}^{\nu_{\text{max}}} \nu B_\nu(T_{\text{hot}}) d\nu. \quad (9)$$

The model SEDs of galaxies with $L_{\text{IR}} = 10^8 L_\odot - 10^{14} L_\odot$ constructed in this manner are shown in Fig. 1. The solid curves represent our model SEDs with various L_{IR} (the lowest one: $L_{\text{IR}} = 10^8 L_\odot$; level interval: $\Delta \log L_{\text{IR}} = 1.0$). We also presented the observed SEDs of three representative IR galaxies, M82 (Klein, Wielebinski, & Morsi 1988), IRAS F10214 + 4724 ($z = 2.286$, Rowan-Robinson et al. 1993), and SMM02399 – 0136 ($z = 2.803$, Ivison et al. 1998). Open triangles stand for the observed SED of M82, open squares depict the SED of IRAS F10214 + 4724, and open diamonds represent the SED of SMM02399 – 0136. Small downward arrows show upper-limit values. The IR luminosity of M82 is $\sim 4 \times 10^{10} L_\odot$ and that of IRAS F10214 + 4724 is $\sim 3 \times 10^{14} L_\odot$, but the latter has been revealed to be magnified by gravitational lensing by a factor of ~ 20 (Broadhurst & Lehár 1995). Its L_{IR} turns out to be $\sim 10^{13} L_\odot$, and its SED is corrected in Fig. 1. SMM02399 – 0136 is also a lensed object, and its unlensed L_{IR} is $\sim 4 \times 10^{13}$ (Ivison et al. 1998). The SED of this galaxy is also corrected for the lensing (by factors of 3.5). Their SEDs are approximately fitted by our models with corresponding L_{IR} .

2.2. Local Luminosity Function

We adopted the LF based on the *IRAS* by Soifer et al. (1987b) as the local IR LF of galaxies. Their LF is defined by $L_{60\mu\text{m}}$, so we converted it into our L_{IR} , using our model SEDs. Then we performed an analytical fitting to the resultant data points, and obtained the following double power-law form for our LF:

$$\log[h_{75}^3 \phi_0(h_{75}^{-2} L_{\text{IR}})] = \begin{cases} 7.9 - 1.0 \log(h_{75}^{-2} L_{\text{IR}}/L_{\odot}) & \text{for } 10^8 L_{\odot} < h_{75}^{-2} L_{\text{IR}} < 10^{10.3} L_{\odot}; \\ 17.1 - 1.9 \log(h_{75}^{-2} L_{\text{IR}}/L_{\odot}) & \text{for } 10^{10.3} L_{\odot} < h_{75}^{-2} L_{\text{IR}} < 10^{14} L_{\odot}; \\ \text{no galaxies} & \text{otherwise,} \end{cases} \quad (10)$$

where ϕ_0 is the number density of galaxies in $\text{Mpc}^{-3} \text{dex}^{-1}$ in case of $h_{75} = 1$, where h_{75} is the Hubble parameter normalized by $75 \text{ km s}^{-1} \text{ Mpc}^{-1}$ (i.e. $h_{75} = H_0/75 \text{ km s}^{-1} \text{ Mpc}^{-1}$). This LF is presented in Fig. 2. We note that, because the volume element (defined in eq.26) depends on H_0^{-3} , luminosity function multiplied by the volume element has no dependence on the Hubble parameter. This means that neither galaxy number count nor the expected redshift distribution depend on the Hubble parameter in the empirical approach. Thus, we do not have to consider the effect of the Hubble parameter in the following analyses.

The faint-end slope of the LF of Soifer et al. (1987b) is much steeper than that derived by Saunders et al. (1990). Little is known about the population which occupies the faint end of the LF. We discuss the effect of it in sections 2.5 and 4.3.

2.3. Treatment of Galaxy Evolution

For galaxy evolution, we deal with the following three cases: (i) no evolution (ii) pure luminosity evolution, and (iii) pure density evolution. We define the LF at z , $\phi(z, L_{\text{IR}})$ in *comoving* volume. Then various types of galaxy evolution are characterized by the form of the functions which represent the relation between $\phi_0(L_{\text{IR}})$ and $\phi(z, L_{\text{IR}})$. We also define cumulative LF at redshift z , $\Phi(z, L_{\text{IR}})$,

$$\begin{aligned} \Phi(z, L_{\text{IR}}) &= \int_{L_{\text{IR}}}^{\infty} \phi(z, L'_{\text{IR}}) d \log L'_{\text{IR}} \\ &= \int_{L_{\text{IR}}}^{L_{\text{IR}, \text{max}}} \phi(z, L'_{\text{IR}}) d \log L'_{\text{IR}}, \end{aligned} \quad (11)$$

where $L_{\text{IR}, \text{max}}$ is the maximum IR luminosity at the epoch.

2.3.1. No evolution

The term “no evolution” means that the luminosity function is independent of z :

$$\phi(z, L_{\text{IR}}) = \phi_0(L_{\text{IR}}). \quad (12)$$

Thus the cumulative LF reduces to

$$\Phi(z, L_{\text{IR}}) = \int_{L_{\text{IR}}}^{\infty} \phi_0(L'_{\text{IR}}) \, d \log L'_{\text{IR}}. \quad (13)$$

Although no evolution model seems to describe an unphysical situation, its prediction acts as a valuable standard baseline from which the various evolutionary differences can be compared.

2.3.2. Pure luminosity evolution

The effect of the luminosity evolution of galaxies is modeled by

$$L_{\text{IR}}(z) = L_{\text{IR}}(0) f(z) \quad , \quad (14)$$

$$f(z) \equiv \exp \left[Q \frac{\tau(z)}{t_{\text{H}}} \right] \quad , \quad (15)$$

where Q , $\tau(z)$ and t_{H} are a parameter defining the magnitude of evolution, look-back time as a function of z , and the Hubble time $1/H_0$. This functional form of evolution is proposed by Broadhurst, Ellis, & Glazebrook (1992). Peacock (1987) derived a useful approximation for the look-back time:

$$\frac{\tau(z)}{t_{\text{H}}} \simeq \frac{1}{\beta} \left(1 - (1+z)^{-\beta} \right), \quad (16)$$

where

$$\beta = 1 + \frac{(2q_0)^{0.6}}{2}. \quad (17)$$

This expression for the look-back time is exact for $q_0 = 0$ and $q_0 = 1/2$ and is accurate within the error of $\lesssim 1\%$ for $q_0 \lesssim 3/2$ (Peacock 1987). The function reduces to the simpler form $f(z) \simeq (1+z)^Q$ at the low- z epoch.

Pure luminosity evolution leads to the following expressions as cumulative LF,

$$\begin{aligned} \Phi(z, L_{\text{IR}}) &= \int_{L_{\text{IR}}}^{\infty} \phi(z, L'_{\text{IR}}) \, d \log L'_{\text{IR}} \\ &= \int_{L_{\text{IR}}/f(z)}^{\infty} \phi_0(\tilde{L}'_{\text{IR}}) \, d \log \tilde{L}'_{\text{IR}} \quad , \end{aligned} \quad (18)$$

$$\tilde{L}_{\text{IR}} = \frac{L_{\text{IR}}}{f(z)}. \quad (19)$$

2.3.3. Pure density evolution

We, here, consider the model that only the comoving number density of galaxies changes as a function of redshift, which is called “pure density evolution”. Pure density evolution is expressed as

$$\phi(z, L_{\text{IR}}) = \phi_0(L_{\text{IR}})g(z). \quad (20)$$

The function $g(z)$ is defined by

$$g(z) \equiv \exp \left[P \frac{\tau(z)}{t_{\text{H}}} \right], \quad (21)$$

where P is a parameter defining the amplitude of evolution. This is the same type of function considered in the previous subsection. We note that this type of galaxy evolution is not aimed at describing the “merging” process. The number count model including merging process is widely discussed by Gardner (1998). The cumulative LF becomes

$$\Phi(z, L_{\text{IR}}) = \int_{L_{\text{IR}}}^{\infty} \phi_0(L'_{\text{IR}})g(z) \, d \log L'_{\text{IR}}. \quad (22)$$

2.4. Galaxy Number Count

Using the above formulae, now we calculate the flux–number relation, or so-called galaxy number count. We assume that galaxies are regarded as point sources (i.e. cosmological dimming of surface brightness is not taken into account). Then the relation between observed flux $S(\nu)$ and emitted monochromatic luminosity $L(\nu)$ is given by

$$S(\nu) = \frac{(1+z)L((1+z)\nu)}{4\pi d_{\text{L}}^2}, \quad (23)$$

where d_{L} is luminosity distance. In the Universe without the cosmological constant Λ , d_{L} is expressed by analytical form, in terms of redshift z , deceleration parameter q_0 and Hubble parameter H_0 (Mattig 1958);

$$d_{\text{L}} = \frac{c}{H_0 q_0^2} [z q_0 + (q_0 - 1)(\sqrt{2q_0 z + 1} - 1)], \quad (24)$$

(c : the velocity of light). When we fix a certain $S(\nu)$, we obtain $L((1+z)\nu)$ by using eq. (23). Then the correspondent $L_{\text{IR}}(S(\nu), z)$ at the redshift z is uniquely determined (see 2.1).

We define $N(> S(\nu))$ as the number of galaxies with a detected flux density larger than $S(\nu)$, then it is formulated as

$$N(> S(\nu)) = \int_{\Omega} d\Omega \int_0^{z_{\max}} dz \frac{d^2V}{dz d\Omega} \int_{L_{\text{IR}}(S(\nu), z)}^{\infty} \phi(z, L'_{\text{IR}}) d \log L'_{\text{IR}} , \quad (25)$$

where $d^2V/dz d\Omega$ is the *comoving* volume element per str per z , which can be expressed in terms of cosmological parameters as

$$\left. \frac{d^2V}{d\Omega dz} \right|_z = \frac{c}{H_0} \frac{d_L^2}{(1+z)^3 \sqrt{1+2q_0 z}} , \quad (26)$$

(e.g. Kolb & Turner 1994). We set z_{\max} as 10.

Next, we formulate the number–flux relation with our evolution models. The no-evolution prediction is as follows:

$$N(> S(\nu)) = \int_{\Omega} d\Omega \int_0^{z_{\max}} dz \frac{d^2V}{dz d\Omega} \int_{L_{\text{IR}}(S(\nu), z)}^{\infty} \phi_0(L'_{\text{IR}}) d \log L'_{\text{IR}} . \quad (27)$$

If pure luminosity evolution takes place, the expected number count is derived from eqs.(18) and (25) ,

$$N(> S(\nu)) = \int_{\Omega} d\Omega \int_0^{z_{\max}} dz \frac{d^2V}{dz d\Omega} \int_{L_{\text{IR}}(S(\nu), z)/f(z)}^{\infty} \phi_0(\tilde{L}'_{\text{IR}}) d \log \tilde{L}'_{\text{IR}} . \quad (28)$$

The expression for pure density evolution is obtained in the same manner;

$$N(> S(\nu)) = \int_{\Omega} d\Omega \int_0^{z_{\max}} dz \frac{d^2V}{dz d\Omega} \int_{L_{\text{IR}}(S(\nu), z)}^{\infty} \phi_0(L'_{\text{IR}}) g(z) d \log L'_{\text{IR}} . \quad (29)$$

2.5. Redshift Distribution

When the flux detection limit $S_{\text{lim}}(\nu)$ is given, the limiting luminosity at redshift z can be obtained by the following process. From equation (23), the limiting monochromatic luminosity $L_{\text{lim}}(\nu_{\text{em}})$, where ν_{em} is the emitted frequency at the rest frame of a galaxy at redshift z , can be calculated as

$$L_{\text{lim}}(\nu_{\text{em}}) = \frac{4\pi d_L^2}{1+z} S_{\text{lim}} \left(\frac{\nu_{\text{em}}}{1+z} \right) . \quad (30)$$

We, then, obtain the total IR luminosity $L_{\text{IR}, \text{lim}}$, which uniquely corresponds to the given $L_{\text{lim}}(\nu_{\text{em}})$, and galaxies with L_{IR} larger than $L_{\text{IR}, \text{lim}}$ are detected. In terms of the derived

$L_{\text{IR,lim}}$, the redshift distribution is formulated as

$$\begin{aligned} \left. \frac{d^2N}{d\Omega dz} \right|_z &= \left. \frac{d^2V}{d\Omega dz} \right|_z \int_{L_{\text{IR,lim}}}^{\infty} \phi(z, L'_{\text{IR}}) d \log L'_{\text{IR}} \\ &= \left. \frac{d^2V}{d\Omega dz} \right|_z \Phi(z, L_{\text{IR,lim}}). \end{aligned} \quad (31)$$

The evolutionary effect can be easily introduced in the redshift distribution by using eqs. (14) or (20), as $\Phi(z, L_{\text{IR}})$ in equation (31), and substituting $L_{\text{IR,lim}}$ instead of L_{IR} .

3. PARAMETERS FOR THE EVOLUTIONARY MODELS

In this section, we estimate the evolutionary parameters P and Q defined in section 2.3 in order to perform our calculation. Then we check the validity and consistency of our predictions by comparison with the *IRAS*- and *ISO*-based number counts and the CIRB spectrum obtained by *COBE*.

3.1. Evolutionary Parameters

We used *IRAS* extragalactic source count data to obtain the values of parameters P and Q . Among *IRAS* bandpasses (12, 25, 60, and 100 μm), the 60- μm band is known to be the most suitable for extragalactic studies, and intensively used in the context of the investigation of galaxies (e.g. Soifer et al. 1987a). Therefore we employed the 60- μm data of *IRAS* galaxies.

We first present the differential flux-number relation of *IRAS* 60- μm databases, *IRAS* Point Source Catalog (*IRAS* PSC) and HH87. This is depicted in Fig. 3. Open squares represent the data points of *IRAS* PSC, and filled squares, HH87. These diagrams are constant against flux if the Universe is static Euclidean and source distribution is homogeneous. The prediction of no-evolution model is also shown in Fig. 3. We perform least-square fitting of our evolutionary models on these data points. When we use all data points with equal weight, the most likely values for the parameters are $(P, Q) = (1.3, 0.7)$ ($q_0 = 0.1$) and $(1.4, 0.8)$ ($q_0 = 0.5$). We obtain higher values $(P, Q) = (2.7, 1.4)$ ($q_0 = 0.1$) and $(2.8, 1.5)$ ($q_0 = 0.5$) when the four statistically poorest points around $\log S [\text{Jy}] \sim -0.5$ are omitted. We adopt the latter for our studies on evolution. We note that the estimation of P and Q depends on the fiducial point which is used to determine the normalization of galaxy counts. Some authors define the parameters P and Q so that the model predictions have the same value of $(dN/dS) S^{2.5}$ at 1 Jy (see

e.g., Fig. 1 of Oliver et al. 1992). The others estimated P and Q by overall fitting, as the same as we did, and did not made such kind of normalization (see e.g., Fig. 5 of Ashby et al. 1996). Therefore our values for P and Q seem smaller than those who adopted the former method, but the effect of the evolution is almost the same. These parameters are summarized in Table 1. They are almost independent of q_0 , at least within the available flux limit of *IRAS* data.

3.2. Galaxy Count : Comparison with *IRAS* and *ISO* Results

We compared our number count predictions with the previous survey results obtained by *IRAS* and *ISO*. In the upper two panels of Fig. 4, the 60- μm number count predictions with two evolutionary models ($q_0 = 0.1$ and 0.5) are presented with the result of QMW *IRAS* galaxy survey (Rowan-Robinson et al. 1991). Within the depth of the QMW catalog there is only a small difference between no-evolution and evolutionary predictions, and the model predictions agree with the observed counts. The evolutionary effect is significant in fainter flux regime (e.g. Bertin, Dennefeld, & Moshir 1997).

Comparison between our 175- μm galaxy number count and the results of the *ISO* Lockman Hole survey (K98) is illustrated in the lower panels of Fig. 4. Source identification and flux calibration contains considerable difficulties, which turned out to be an uncertainty of the number count by a few factors. Both *IRAS* and *ISO* number counts are successfully reproduced by our model calculations.

3.3. Cosmic Infrared Background

The CIRB is generated from the integrated light of galaxies. Therefore, combining the SEDs of galaxies and number count predictions, we obtain the CIRB spectrum. The observed flux density of a galaxy whose IR luminosity is L_{IR} , $S(\nu, L_{\text{IR}})$ is given by equation (23) as follows:

$$S(\nu, L_{\text{IR}}) = \frac{(1+z)L(\nu(1+z), L_{\text{IR}})}{4\pi d_L^2}, \quad (32)$$

where $L(\nu, L_{\text{IR}})$ is the monochromatic luminosity of a galaxy with L_{IR} . Then the CIRB spectrum $I(\nu)$, i.e., the background flux density from unit solid angle, is expressed as

$$I(\nu) = \int_0^{z_{\text{max}}} dz \frac{d^2V}{dz d\Omega} \int_0^\infty \phi(z, L'_{\text{IR}}) S(\nu, L'_{\text{IR}}) d \log L'_{\text{IR}}. \quad (33)$$

We can deal with the evolutionary effect on $I(\nu)$ through $\phi(z, L_{\text{IR}})$, just the same as in the case of number count calculation. The expected CIRB spectra are presented in Fig. 5. The upper panel shows the case of $q_0 = 0.1$, and lower panel, $q_0 = 0.5$. We also put the observational constraints on $I(\nu)$ obtained by *COBE* measurement in Fig. 5. Red open triangles represent the “dark sky” upper limit to the CIRB measured by *COBE* Diffuse Infrared Background Experiment (DIRBE). The DIRBE sky brightness varies roughly sinusoidally over the year, due to the complex features of the interplanetary dust cloud. The “dark sky” brightness is that of the darkest area on the sky at each wavelength. Filled squares are the result of a similar analysis of the *COBE* Far Infrared Absolute Spectrophotometer (FIRAS) high-frequency data, after removal of the CMB (cosmic microwave background) signal. The dark sky values of DIRBE and FIRAS show excellent agreement with each other. Blue open triangles represent the residual signal of DIRBE after removing the contributions from the model foreground sources such as Galactic diffuse emission, and interplanetary dust emission. As described by Mather et al.(1994), the CMB spectrum in the wavelength range 0.5 – 5 mm deviates from a 2.726 K-blackbody shape by less than 0.03 % of the peak intensity. This deviation is shown by green horizontal lines. Details of these background signals are summarized in Hauser (1995). In addition, Puget et al. (1996) have reported the isotropic diffuse residual light of FIRAS data, after subtracting the foreground contributions. Fixsen et al. (1998) and Hauser et al. (1998) have also reported similar results. The orange broken solid lines are the approximate shape of the spectrum of the residual light reported by Puget et al., Fixsen et al., and Hauser et al. with errors.

Within the wavelengths shorter than 300 μm , our model prediction is consistent with the CIRB intensity, but in the longer wavelengths, it seems to violate the limits from the CIRB (larger q_0 mitigates this discrepancy). In such a long wavelength regime, the background radiation is dominated by the contributions from hyperluminous IR galaxies at very high redshifts. As we see from Fig. 1, the SEDs of such luminous galaxies are well represented by our SED models. Thus, the functional form of the galaxy evolution might be too simple and possibly not valid in extremely high- z objects, or alternatively, high-luminosity end of the LF might not be valid at high- z . In spite of the difficulty in sub-mm range, our model works for our present purpose which is IR source number count prediction in wavelength region shorter than 300 μm .

4. RESULTS AND DISCUSSIONS

4.1. *IRIS* Survey Performance

4.1.1. Flux Detection Limit of IRIS FIS

The flux detection limit $S_{\text{lim}}(\nu)$ is decided by some factors; the sensitivity of the device, the intervening emission, e.g. zodiacal light, interstellar emission of Our Galaxy, and source confusion etc. The dominant factor is different in different wavebands, and the resultant $S_{\text{lim}}(\nu)$ is dependent on wavelength. Thus the calculation requires the careful consideration of $S_{\text{lim}}(\nu)$ individually for each λ or ν . We assume 50-, 70-, 120-, and 150 μm bandpasses for *IRIS* FIS. Unstressed gallium-doped germanium (Ge:Ga) is used for the shorter wavelength in FIR (50 – 110 μm) and stressed Ge:Ga for the longer wavelength ($\lesssim 170 \mu\text{m}$) (Kawada et al. 1998). In the shorter wavelength, sensitivity is limited by internal and background noises, while in the longer wavelength, it is constrained by the source and Galactic cirrus confusion (Gautier et al. 1992; Thronson et al. 1995). The resultant 5σ -detection limits of the assumed four wavebands are summarized in Table 2².

4.1.2. IRIS galaxy number count predictions

Our predictions for the galaxy number count at assumed *IRIS* four bandpasses are shown in Fig. 6. The upper four panels depict the number counts with $q_0 = 0.1$ and the lower four, $q_0 = 0.5$; from left to right, $\lambda = 50, 70, 120,$ and $150 \mu\text{m}$. The black solid lines show the no-evolution prediction. The red and cyan lines represent the case of pure luminosity evolution and pure density evolution, respectively. The green dot-dashed lines in Fig. 6 denote the *IRIS* FIS flux detection limit at each band. The integrated detection number to the flux limit of each bandpass is $\sim 10^5 \text{ str}^{-1}$ at 50 μm , $\sim 2 \times 10^5 \text{ str}^{-1}$ at 70 μm , $\sim 3 \times 10^5 \text{ str}^{-1}$ at 120 μm , and $\sim 2 \times 10^5 \text{ str}^{-1}$ at 150 μm in the case of no evolution, thus the expected detection number is largest at 120 μm , and the total number of galaxy is expected to be $\sim \text{several} \times 10^6$ in the whole sky. This is about 100-times larger than the number of *IRAS* galaxies, which is ~ 25000 in all the sky. It is clearly seen that q_0 does not affect the number count within the detectable flux range of *IRIS* as shown in Fig. 6.

The effect of evolution appears most significantly at 70 μm among the assumed bands, and the total detection number becomes twice larger. Thus, the determination of the amplitude of galaxy evolution is best estimated at around 70 μm in the wavelength and

²The flux detection limits presented here are based on those in Kawada et al. (1998), but are slightly (by a factor of 1.5 – 2) deeper than the limits they reported; the values adopted here are those expected in the high Galactic latitude region ($|b| > 60^\circ$). Much better point source detection limits can be expected in limited sky areas near the ecliptic poles, where the survey scan will be repeated more than hundred times, and can be achieved by a spatial deconvolution algorithm.

flux coverage of *IRIS*. With the aid of such a vast number of galaxy detections, we will be able to evaluate the evolution strength (P or Q) precisely. In the case of 70- μm band, statistical fluctuation becomes much smaller than those of previous area-limited deep surveys. Consequently the errors in the estimation of P or Q will be small enough, at least, to determine them in the relatively low-redshift ($z \lesssim 1$) universe. Unfortunately, there exists no drastic difference between luminosity and density evolution in the behaviors of number count, and judging which evolution takes place from number count alone still remains as a difficult work.

4.2. Redshift Distribution

Using the *IRIS* FIS flux detection limits we gave in section 4.1.1, we calculate the redshift distribution of galaxies detected by the *IRIS* all-sky survey. Figure 7 shows the expected redshift distribution of galaxies detected in the assumed four bands. Figure 7a illustrates the prediction at 50- μm band. Figures 7b, 7c, and 7d are the same as Fig. 7a, except that they show the predictions at 70-, 120-, and 150- μm bands, respectively. Solid curves denote the predictions for $q_0 = 0.1$, and dashed curves, $q_0 = 0.5$. Larger q_0 leads to deeper z -distribution. In any bandpasses, the numbers of galaxies at $z \gtrsim 1$ are \sim a few $\times 10^3$, and several times larger with evolution. Namely, low- z galaxies are the overwhelming majority among the detected objects. The steep increases of galaxy number at $z \lesssim 0.5$ seen in Figs. 7c and 7d are attributed to the peak at $\sim 100 \mu\text{m}$, which originates from big grains, in the SED of low- L_{IR} ($L_{\text{IR}} \lesssim 10^{11} L_{\odot}$) galaxies. Figure 8 is an example of the redshift distribution for detected galaxies with various L_{IR} ($q_0 = 0.1$, no evolution). Such galaxies can be detected only within $z \lesssim 0.5$. The LF we employed makes them to be abundant; if we use flatter faint-end slope of the LF, the increases would be less prominent.

The overall shape of the redshift distribution depends on the observing bandpass wavelength. Nearest galaxies ($z \sim 0 - 0.5$) are more likely to be detected in longer wavelength $\lambda = 120 - 150 \mu\text{m}$, and their detection number steeply decreases with increasing z in the longest wavelengths. Galaxies which lie within the redshift range of $z \sim 0.5 - 2.5$ are expected to be detected more at 70 μm than at the other bands. When the galaxy redshift exceeds ~ 3 , they become harder to be detected in the shorter bands, while they remain detectable in the longer bands. The detection numbers at $\lambda = 120 \mu\text{m}$ and 150 μm , therefore, surpass those at $\lambda = 50 \mu\text{m}$ and 70 μm for the furthest galaxies. This is understood as follows. At significant redshift ($z \gtrsim 3$), the detected objects are the most luminous starbursts, whose SEDs peak at around 30 μm in the rest frame. Since the peaks of luminous starbursts shift away from their rest wavelength, they are not detected at

high- z in shorter wavelengths. Instead, in the longer wavebands, redshift effect makes their observed flux density nearly constant (known as the negative K -correction), and they can be still seen at high- z .

4.3. Color–color Diagram in FIR

As we saw in section 4.2, most of the objects detected in the *IRIS* galaxy survey are nearby ones. Hence, when we focus on the very young or primeval galaxies, an efficient method to pick up such candidates without knowing their spectroscopic redshifts will be very useful. We, here, make attempts to utilize the peaks of the SEDs to estimate the redshifts roughly from their FIR colors alone. We suppose that all the Galactic objects are taken away by certain methods. This may well be possible at high Galactic latitudes.

Figure 9 shows the loci of galaxies with various L_{IR} on the FIR color–color ($\log S_{50}/S_{70} - \log S_{50}/S_{150}$) plane, where S_{λ} is the detected flux density of galaxies at wavelength λ [μm] in unit of [$\text{erg s}^{-1}\text{cm}^{-2}\text{Hz}^{-1}$]. Filled symbols are put on every $\Delta z = 0.5$ interval from $z = 0$. When the sources fade away from the *IRIS* detection limits, we do not show their loci and symbols. Red filled squares represent the colors of the low- z ($z < 1$) galaxies, green filled squares the intermediate- z ($1 < z < 2.5$), and blue filled circles the high- z ($2.5 < z$) ones. Because of the way of the construction of our model SEDs, galaxies with $L_{\text{IR}} = 10^8 - 10^{10} L_{\odot}$ have the same colors (the red filled square at the top-right). To see how the existence of starburst component changes the color of cool cirrus galaxies, we put the galaxies of $L_{\text{IR}} = 10^{10.1} L_{\odot} - 10^{10.9} L_{\odot}$ with an interval of $\Delta \log L_{\text{IR}} = 0.1$ (denoted by open squares from the top-right to down-left). They correspond to the galaxies whose IR luminosity fraction of the superposed starburst is 20.6, 36.7, 50.0, 60.2, 68.4, 74.9, 80.0, 84.2, and 87.4 %, respectively.

When we consider the color selection criteria, the intrinsic scatter of galaxy color has to be taken into account. Schmitt et al. (1997) proposed the template SEDs of various classes of galaxies. Their SEDs show that the dispersion at FIR wavelength is an order unity. The scatter of *IRAS* S_{100}/S_{60} is also known to be an order of magnitude (RC89). Considering these scatters, we can estimate the domains where galaxies locate on the FIR color-color plane. We show the the domains of low- ($z < 1$), intermediate- ($1 < z < 2.5$) and high- z ($z > 2.5$) galaxies with a red dashed rhomboid, a green solid rectangle, and a blue solid rectangle, respectively. The high- z and mid- z regions are well separated on this diagram.

We must think of the overlap between low- z and mid/high- z domains. The low- z population creeping in the mid/high- z domain consists of only low- L_{IR} galaxies

($L_{\text{IR}} \lesssim 10^{11} L_{\odot}$). As we have seen in section 4.2, such galaxies quickly become undetectable with increasing redshift and reside in $z \lesssim 0.2$. The expected optical magnitude based on SEDs extended to optical region ranges from ~ 17 mag to ~ 19 mag (Hirashita et al. 1998). Since the positional accuracy of the *IRIS* survey is quite good ($5'' - 10''$) and surface density of such bright galaxies is low enough, these galaxies would be identified easily with optical counterparts. On the contrary, the high- z galaxies are expected to have fainter magnitudes (~ 20 mag) (Hirashita et al. 1998). Thus the cross correlation with optical survey data such as POSS, or forthcoming SDSS would identify most of the low- z IR-galaxies. Evolutionary effect makes the mid/high- z galaxy more abundant, and the fraction of such objects in the overlapped region will be higher. Thus, color classification of galaxy redshift can be practicable using sets of bandpasses 50, 70, and 150 μm with the aid of present and future optical surveys.

5. SUMMARY AND CONCLUSIONS

In this paper we examined the performance of the *IRIS* FIR all-sky survey, one of whose main purposes is to study galaxy evolution and formation. We used a simple empirical model for galaxy number count estimation, by adopting a multicomponent SED model which consists of cirrus and starburst components, and the nearby FIR luminosity function derived from that of *IRAS* galaxies.

Our conclusions are as follows:

1. A few $\times 10^6$ galaxies will be detected by the *IRIS* all-sky survey, which is 100 times larger number of detection than that of *IRAS*.
2. Shorter wavelength bandpass (50 – 70 μm) is suitable for intermediate- z ($1 < z < 2.5$) galaxy detection, while longer wavelength (120 – 150 μm) one is for high- z ($2.5 < z$) and nearby ($z < 1$) galaxies.
3. We will detect the effect of galaxy evolution and can evaluate the amplitude of evolution at least in the nearby universe in the *IRIS* survey, but still it is difficult to constrain which type of evolution takes place, from the number count alone. On the contrary, the intensity of the CIRB complementarily provides us much tighter constraint on the form of galaxy evolution at very high- z .
4. Redshift estimation using galaxy FIR colors can be practicable using sets of bandpasses 50, 70, and 150 μm with the aid of present and future optical surveys.

We first thank the anonymous referee for valuable suggestions and corrections which improved the paper much. We owe a great debt to Drs. Hideo Matsuhara, Takao Nakagawa, Mitsunobu Kawada, and other members of the *IRIS* mission for useful discussions and comments. We also acknowledge Drs. Chris P. Pearson, Gavin Dalton, Toru Yamada, Kimiaki Kawara for fruitful discussions. We offer our gratitude to Profs. Mamoru Saitō, Hiroki Kurokawa, and Shin Mineshige for continuous encouragement. Two of us (TTT and HH) acknowledge the Research Fellowships of the Japan Society for the Promotion of Science for Young Scientists. This research has also made use of the NASA/IPAC Extragalactic Database (NED) which is operated by the Jet Propulsion Laboratory, California Institute of Technology, under contract with the National Aeronautics and Space Administration. We also made extensive use of the NASA’s Astrophysics Data System Abstract Service (ADS).

A. APPENDIX : OTHER FUTURE MISSIONS

We show the expected number counts and redshift distributions of galaxies in other future missions now planned, *SOFIA*, *SIRTF*, *FIRST*, and *LMSA*. The present model is valid only within the mid-IR to sub-mm wavelengths because of the SED used, we restrict the count predictions within this range. We calculated the number counts and redshift distributions in the same way as we did in the main text. In this appendix, we only consider the case of $q_0 = 0.1$ cosmology with pure luminosity evolution ($Q = 1.4$). Though some of the facilities are not planned to be used for large-area survey, we uniformly calculated the number counts per unit solid angle, and the redshift distributions in the whole sky. We applied the detection limits from published papers or from the web pages of the missions if available.

A.1. *SOFIA*

Stratospheric Observatory for Infrared Astronomy (*SOFIA*) is an airborne observatory with a 2.5-meter telescope installed in a Boeing 747 aircraft, which will be flying in 2001. The detection limits (1σ noise level) for 1 hour exposure are 7 mJy at $100 \mu\text{m}$ and 3.5 mJy at $450 \mu\text{m}$ (Becklin 1997). Based on these values we calculated the number count and redshifts with 5σ -detection limits (obtained by simply multiplying factor 5 to the above limits). The galaxy number counts are presented in the upper-left panel of Fig. 10, and the redshift distributions are shown in the upper-left panel of Fig. 11.

A.2. *SIRTF*

The Space Infrared Telescope Facility (*SIRTF*) is the 4th and final element in NASA’s family of “Great Observatories”. *SIRTF* consists of a 0.85-meter telescope and three cooled instruments, IRAC, MIPS, and IRS, capable of performing imaging and spectroscopy in the 3 – 180 μm wavelength range. It is planned to be launched in December 2001. We present the predictions for MIPS (Multiband Imaging Photometer for *SIRTF*) at wavelengths 23.5, 70, and 160 μm . The 5σ -detection limits are 370 μJy , 1.4 mJy, and 7.5 mJy, respectively, by 500-s exposure (Heim et al. 1998). *SIRTF* will survey 60 % of the whole sky. The upper-left panel of Fig. 10 depicts the number counts, and the upper-left panel of Fig. 11 shows the redshift distribution.

A.3. *FIRST*

The Far Infrared and Submillimetre Telescope (*FIRST*) is the 4th cornerstone mission in the European Space Agency’s Horizons 2000 programme, implemented in collaboration with NASA. *FIRST* will perform photometry and spectroscopy in the 80 – 670 μm range. Three instruments have been provisionally selected: HIFI, PACS, and SPIRE. Imaging photometry is performed by PACS (80 – 210 μm) and SPIRE (200 – 670 μm). The 5σ -detection limits (by 1 hour exposure) for PACS and SPIRE are 5 mJy and 3 mJy, respectively (Pilbratt 1998). We show 90- μm number count for PACS and 250, 350, and 500 μm for SPIRE in the lower-left panel of Fig. 10. Redshift distributions of the objects detected at these bandpasses are presented in the lower-left panel of Fig. 11.

A.4. *LMSA*

The Large Millimeter and Submillimeter Array (*LMSA*) is the ground-based radio facility proposed in Japan. In the current design concept the array will consist of 50 10-m antennas and will be covering observing frequencies from 80 to 800 GHz. The array will be located at very high site to realize sub-arcsec resolution imaging at very high frequencies. We present the number counts expected by *LMSA* at 350, 450, 650, and 850 μm . The 5σ sensitivities at these wavelengths (yearly mean values) are 3350, 1800, 750, and 115 $\mu\text{Jy}/\text{beam}$, respectively, by 8-hour integration (Kawabe & Kohno 1998, private communication). Under the best weather condition in winter, much higher sensitivities can be achieved. The galaxy number counts are shown in the lower-right panel of Fig. 10. The lower-right panel of Fig. 11 illustrates the expected redshifts. In the lower-right panel of

Fig. 10, we compared our prediction with the 850 μm number counts recently obtained by *SCUBA* in JCMT. Filled red circle represents the value obtained by Smail et al. (1998), filled square shows the result in Hubble Deep Field (Hughes et al. 1998), and filled triangle is the number count in Lockman Hole (Barger et al. 1998). In spite that we include the evolution in this calculation, our prediction is an order of magnitude smaller than those results. Thus, a very strong evolution is suggested by sub-mm observations. It requires further detailed analyses of the present observational data to study the history of galaxy evolution in wide range of wavelength.

REFERENCES

- Ashby, M. L. N., Hacking, P. B., Houck, J. R., Soifer, B. T., & Weisstein, E. W. 1996, *ApJ*, 456, 428
- Barger, A. J., Cowie, L. L., Sanders, D. B., Fulton, E., Taniguchi, Y. Y., Sato, Y, Kawara, K., & Okuda, H. 1998, *Nature*, 394, 248
- Becklin, E. E. 1997, in *The Far Infrared and Submillimetre Universe*, ESA publication, ESA SP0401, ed. Wilson, A., & Noordwijk, p201
- Beichman, C. A. & Helou, G. 1991, *ApJ*, 370, L1 (BH91)
- Bertin, E., Dennefeld, M., & Moshir, M. 1997, *A&A*, 323, 685
- Bond, J. R., Carr, B. J., & Hogan, C. J. 1986, *ApJ*, 306, 428
- Boulanger, F., Baud, B., van Albada, G. D. 1985, *A&A*, 144, L9
- Broadhurst, T. J., Ellis, R. S., & Glazebrook, K. 1992, *Nature*, 355, 55
- Broadhurst, T. J., & Lehár, J. 1995, *ApJ*, 450, L41
- Burigana, C., Danese, L., De Zotti, G., Franceschini, A., Mazzei, P., & Toffolatti, L. 1997, *MNRAS*, 287, L17
- Désert, F.-X., Boulanger, F., & Puget, J. -L. 1990, *A&A*, 237, 215
- Draine, B. T. & Anderson, N. 1985, *ApJ*, 292, 494
- Eales, S. A., & Edmunds, M. G. 1997, *MNRAS*, 186, 732
- Ebbels, T. M. D., Le Borgne, J. -F., Pelló, R., Ellis, R. S., Kneib, J. -P., Smail, I., & Sanahuja, B. 1996, *MNRAS*, 281, L75
- Ellis, R. S., Colless, M., Broadhurst, T. J., Heyl, J., & Glazebrook, K. 1996, *MNRAS*, 280, 235
- Ellis, R. S. 1997, *ARA&A*, 35, 389
- Fixsen, D. J., Dwek, E., Mather, J. C., Bennet, C. L., & Shafer, R. A. 1998, *ApJ*, in press, astro-ph/9803021
- Franceschini, A., Mazzei, P., De Zotti, G., & Danese, L. 1994, *ApJ*, 427, 140

- Franx, M., Illingworth, G. D., Kelson, D. D., van Dokkum, P. G., & Tran, K. -V. 1997, ApJ, 486, L75
- Gardner, J.P. 1998, PASP, 110, 291
- Gautier, T. N.,III, Boulanger, R., Péroult, M., & Puget, J. L. 1992, AJ, 103, 1313
- Guiderdoni, B., Hivon, E., Bouchet, F. R., & Maffei, B. 1997, MNRAS, 295, 877
- Hacking, P. B., Condon, J. J., & Houck, J. R. 1987, ApJ, 316, L15
- Hacking, P. B., & Houck, J. R. 1987, ApJS, 63, 311 (HH87)
- Hauser, M. G. 1995, in *Unveiling the Cosmic Infrared Background*, E. Dwek (ed.), AIP, pp11 – 21
- Hauser, M. G., et al. 1998, ApJ, in press, astro-ph/9806167
- Heim, G. B., et al. 1998, in *Space Telescopes and Instruments V*, SPIE, Vol. 3356, in press
- Helou, G. 1986, ApJ, 311, L33
- Hirashita, H., Takeuchi, T. T., Ohta, K., & Shibai, H. 1998, PASJ, submitted
- Hughes, D., et al. 1998, Nature, 394, 241
- IRAS Point Source Catalog*, 1985, Joint *IRAS Science Working Group* (GPO, Washington, DC) (*IRAS PSC*)
- Iverson, R. J., Smail, I., Le Borgne, J. -F., Blain, A. W., Kneib, J. -P., Bézecourt, J., Kerr, T. H., & Davies, J. K. 1998, MNRAS, 298, 583
- Kawada, M., et al. 1998, in *Infrared Astronomical Instrumentation*, Proc. SPIE, in press
- Kawara, K., et al. 1998, A&A, 336, L9 (K98)
- Kennicutt, R. C., Jr., Tamblyn, P., & Congdon, C. E. 1994, ApJ, 435, 22
- Kessler, M. et al. 1996, A&A, 315, L27
- Klein, U., Wielebinski, R., & Morsi, H. W. 1988, A&A, 190, 4
- Kolb, E. W., & Turner, M. S. 1994, *The Early Universe*, Addison Wesley
- Lilly, S.J, Le Fèvre, O., Hammer, F., & Crampton, D. 1996, ApJ, 460, L1

- Lowenthal, J. C., Koo, D. C., Guzmán, R., Gallego, J., Phillips, A. C., Faber, S. M., Vogt, N. P., Illingworth, G. D., & Gronwall, C. 1997, *ApJ*, 481, 673
- Madau, P., Ferguson, H. C., Dickinson, M. E., Giavalisco, M., Steidel, C. C., & Fruchter, A. 1996, *MNRAS*, 283, 1388
- Mather, J. C., et al. 1994, *ApJ*, 420, 439
- Mattig, W. 1958, *Astr. Nachr.*, 284, 109
- Ohta, K., Yamada, T., Nakanishi, K., Kohno, K., Akiyama, M., & Kawabe, R. 1996, *Nature*, 382, 426
- Oliver, S. J., Rowan-Robinson, M., & Saunders, W. 1992, *MNRAS*, 256, 15P
- Oliver, S. J., et al., 1997, *MNRAS*, 289, 471
- Omont, A., Petitjean, P., Guilloteau, S., McMahon, R. G., Solomon, P. M., & Pecontal, E. 1996, *Nature*, 382, 428
- Peacock, J. A. 1987, in *Astrophysical Jets and their Engines*, W. Kundt (ed.), Reidel: Dordrecht, p171
- Pearson, C. P. 1996, Ph.D thesis
- Pearson, C. P., & Rowan-Robinson, M. 1996, *MNRAS*, 283, 174
- Pilbratt, G. 1998, <http://astro.estec.esa.nl/First>
- Puget, J. -L., Abergel, A., Bernard, J. -P., Boulanger, F., Burton, W. B., Désert, F. -X., & Hartmann, D. 1996, *A&A*, 308, L5
- Rieke, G. H., & Lebofsky M. J. 1986, *ApJ*, 304, 326
- Rowan-Robinson, M. 1986, *MNRAS*, 219, 737
- Rowan-Robinson, M. 1992, *MNRAS*, 258, 787
- Rowan-Robinson, M. & Crawford, J. 1989, *MNRAS*, 238, 523 (RC89)
- Rowan-Robinson, M., Saunders, W., Lawrence, A., & Leech, K. 1991, *MNRAS*, 253, 485
- Rowan-Robinson, M., et al. 1993, *MNRAS*, 261, 513
- Sanders, D. B., & Mirabel, I. F. 1996, *ARA&A*, 34, 749

- Saunders, W., Rowan-Robinson, M., Lawrence, A., Efsthathiou, G., Kaiser, N., Ellis, R. S., & Frenk, C. S. 1990, *MNRAS*, 242, 318
- Schmitt, H. R., Kinney, A. L., Calzetti, D., & Storchi-Bergmann, T. 1997, *AJ*, 144, 592
- Smail, I., Ivison, R. J., & Blain, A. W. 1998, *ApJ*, 490, L5
- Soifer, B. T., Houck, J. R., & Neugebauer, G. 1987a, *ARA&A*, 25, 187
- Soifer, B. T., Sanders, D. B., Madore, B. F., Neugebauer, G., Danielson, G. E., Elias, J. H., Lonsdale, C. J., & Rice, W. L. 1987b, *ApJ*, 320, 238
- Steidel, C. C., Pettini, M., & Hamilton, D. 1995, *AJ*, 110, 2519
- Steidel, C. C., Giavalisco, M., Pettini, M., Dickinson, M., & Adelberger, K. L. 1996, *ApJ*, 462, L17
- Thronson, H. A., Rapp, D., Bailey, B., & Hawarden, T. G. 1995, *PASP*, 107, 1099
- Trager, S. C., Faber, S. M., Dressler, A., & Oemler, A., Jr. 1997, *ApJ*, 485, 92
- Trayer, M.-A., & Silk, J. 1993, *ApJ*, 408, L1
- Tresse, L., & Maddox, S. J. 1998, *ApJ*, 495, 691
- Yee, H. K. C., Ellingson, E., Bechtold, J., Carlberg, R. G., & Cuillandre, J. -C. 1996, *AJ*, 111, 1783

Figure Captions

Fig. 1.— The model spectral energy distributions (SEDs) of galaxies with $L_{\text{IR}} = 10^8 L_{\odot} - 10^{14} L_{\odot}$. The solid curves represent our model SEDs with various L_{IR} (the lowest one: $L_{\text{IR}} = 10^8 L_{\odot}$; level interval: $\Delta \log L_{\text{IR}} = 1.0$). We also present the observed SEDs of two representative IR galaxies, M82 (Klein, Wielebinski, & Morsi 1988), IRAS F10214+4724 (Rowan-Robinson et al. 1993), and SMM02399 – 0136 (Ivison et al. 1998). Open triangles stand for the observed SED of M82, open squares depict the SED of IRAS F10214 + 4724, and open diamonds represent the SED of SMM02399 – 0136. Small downward arrows show upper-limit values. The IR luminosity of M82 is $\sim 4 \times 10^{10} L_{\odot}$ and that of IRAS F10214+4724 is $\sim 3 \times 10^{14} L_{\odot}$, but the latter has been revealed to be magnified by gravitational lensing by a factor of ~ 20 (Broadhurst & Lehár 1995). Its L_{IR} turns out to be $\sim 10^{13} L_{\odot}$, and its SED is corrected in this figure. SMM02399 – 0136 is also a lensed object, and its unlensed L_{IR} is $\sim 4 \times 10^{13}$ (Ivison et al. 1998). The SED of this galaxy is also corrected for the lensing. Their SEDs are approximately fitted by our models with corresponding L_{IR} .

Fig. 2.— The local infrared luminosity function (LF) of galaxies $\phi_0(L_{\text{IR}})$. This is constructed from the LF of Soifer et al. (1987b). Since their LF is defined by $L_{60\mu\text{m}}$, we converted it into L_{IR} (the IR luminosity in the wavelength range of $3 \mu\text{m} - 1 \text{mm}$), using our model SEDs. The filled squares represent the converted data points, and solid line stands for the fitted analytical function presented in the main text (see eq. 10). Dotted line is shown for the L_{IR} of the ‘knee’ of our LF.

Fig. 3.— The differential flux-number relation for *IRAS* 60- μm databases and our model predictions. Open squares represent the data points for *IRAS* PSC, and filled squares, HH87. The no-evolution model tracks are also shown by black solid curves. Upper panel shows the case of $q_0 = 0.1$, and lower panel, of $q_0 = 0.5$. We performed least-square fitting of our evolutionary models (see section 2.3) on these data points. When we adopt all data points with equal weight, the most likely value for the parameters are $(P, Q) = (1.3, 0.7)$ ($q_0 = 0.1$) and $(1.4, 0.8)$ ($q_0 = 0.5$). We obtain higher values $(P, Q) = (2.7, 1.4)$ ($q_0 = 0.1$) and $(2.8, 1.5)$ ($q_0 = 0.5$) when the four statistically poorest points around $\log S [\text{Jy}] \sim -0.5$ are removed. We adopt the latter in our studies.

Fig. 4.— The integrated galaxy number count ($q_0 = 0.1$ and 0.5) at 60- μm and 175- μm . The results of QMW *IRAS* galaxy survey (Rowan-Robinson et al. 1991) and the *ISO* Lockman Hole survey (Kawara et al. 1998) are also presented. The upper panels represents the 60- μm prediction. The agreement of the model and the QMW count is excellent. The lower panels shows the 175- μm number count. The horizontal errors are caused by the uncertainty of flux calibration. Within the error, the model agrees with the *ISO* result.

Fig. 5.— The expected cosmic infrared background (CIRB) spectra with $q_0 = 0.1$ and $q_0 = 0.5$. The background intensity depends on q_0 , so that larger q_0 leads to smaller $I(\nu)$. We also put the observational constraints on CIRB obtained by *COBE* measurement. Open red triangles represent the “dark sky” (see section 3.3) upper limit to the CIRB measured by *COBE* Diffuse Infrared Background Experiment (DIRBE). Filled squares are the result of a similar analysis of the *COBE* Far Infrared Absolute Spectrophotometer (FIRAS) high-frequency data, after removal of the cosmic microwave background signal. Open blue triangles represent the residual signal of DIRBE after removing the contributions from the model foreground sources such as Galactic diffuse emission, and interplanetary dust emission. The green horizontal lines represent the upper limit derived from Mather et al. (1994), and solid orange broken lines represent the approximate value of the residual light reported by Puget et al. (1996), Fixsen et al. (1998) and Hauser et al. (1998) with errors. The CIRB constraint on the magnitude of galaxy evolution is tighter than that obtained from the number count.

Fig. 6.— The galaxy number count predictions at assumed *IRIS* four bandpasses. The upper four panels depict the number counts with $q_0 = 0.1$ and the lower four, $q_0 = 0.5$; from left to right, $\lambda = 50, 70, 120,$ and $150 \mu\text{m}$. The black solid lines show the no-evolution prediction. The red lines and cyan lines represent the case of pure luminosity evolution and pure density evolution, respectively. The green dot-dashed lines denote the *IRIS* FIS flux detection limit at each waveband.

Fig. 7.— The expected redshift distribution of galaxies detected in the assumed four bands. Figure 7a illustrates the prediction at $50\text{-}\mu\text{m}$ band. Figures 7b, 7c, and 7d are the same as Fig. 7a, except that they show the predictions at $70\text{-}, 120\text{-},$ and $150\text{-}\mu\text{m}$ bands, respectively. Solid curves denote the predictions for $q_0 = 0.1$, and dashed curves, $q_0 = 0.5$. Larger q_0 leads to deeper z -distribution. The steep increases of galaxy number at $z < 0.5$ seen in Figs. 7c and 7d are attributed to the peak at $\sim 100 \mu\text{m}$, which originates from big grains, in the SED of low- L_{IR} galaxies.

Fig. 8.— An example of the redshift distribution of detected galaxies with various L_{IR} ($q_0 = 0.1$, no evolution). Solid curves represent the galaxies with low- L_{IR} , dashed curves the intermediate- L_{IR} , and dot-dashed curves the high- L_{IR} .

Fig. 9.— The loci of galaxies with various L_{IR} on the FIR color-color ($\log S_{50}/S_{70} - \log S_{50}/S_{150}$) plane. Filled squares are put on every $\Delta z = 0.5$ interval. Red filled squares represent the colors of the low- z ($z < 1$) galaxies, green filled squares the intermediate- z ($1 < z < 2.5$), and blue filled squares the high- z ($2.5 < z$) ones. For the sources fade away from the *IRIS* detection limits, we do not show their loci and symbols. To

see how the starburst changes the color of cool cirrus galaxies, we put the galaxies of $L_{\text{IR}} = 10^{10.1} L_{\odot} - 10^{10.9} L_{\odot}$ with an interval of $\Delta \log L_{\text{IR}} = 0.1$ (denoted by red open squares from the top-right to down-left). The domain which is occupied mainly by low- z , low- L_{IR} galaxies are shown roughly by red dotted rhomboid. Green rectangle shows the domain of intermediate- z ones, and blue rectangle shows the region where high- z galaxies to be located.

Fig. 10.— Integrated number counts of galaxies expected for *SOFIA*, *SIRTF*, *FIRST*, *LMSA*. *SOFIA* (upper-left) : Blue and red solid lines represent our 120 μm and 450 μm predictions, respectively. The vertical blue and red dot-dashed lines show the 5σ -detection limit of *SOFIA* with 1-hour exposure. We adopted $q_0 = 0.1$ with pure luminosity evolution ($Q = 1.4$) in this and the following figures. *SIRTF* (upper-right) : Integrated number counts of galaxies expected for *SIRTF*. Blue, green, and red solid lines represent our 25, 70, and 160 μm predictions, respectively. The vertical blue, green, and red dot-dashed lines show the 5σ -detection limit of *SIRTF* MIPS with 500-s exposure. *FIRST* (lower-left) : Integrated number counts of galaxies expected for *FIRST*. Blue, green, yellow and red solid lines represent our 90, 250, 350, and 500 μm predictions, respectively. The vertical blue, green, yellow and red dot-dashed lines show the 5σ -detection limit of *FIRST* PACS (90 μm) and SPIRE (250, 350, and 500 μm) with 1-hour exposure. *LMSA* (lower-right) : Integrated number counts of galaxies expected for *LMSA*. Blue, green, yellow and red solid lines represent our 350, 450, 650, and 800 μm predictions, respectively. The vertical blue, green, yellow and red dot-dashed lines show the 5σ -detection limit of *LMSA* with 8-hour exposure. Filled red circle represents the galaxy number count reported by Smail et al. (1998), filled square shows the result in Hubble Deep Field (Hughes et al. 1998), and filled triangle is the count in Lockman Hole (Barger et al. 1998), all obtained with *SCUBA* in JCMT at 850 μm .

Fig. 11.— The redshift distribution of galaxies detected with *SOFIA*, *SIRTF* MIPS, *FIRST*, and *LMSA* assuming the whole-sky observation; upper-left : *SOFIA*, upper-right : *SIRTF*, lower-left : *FIRST*, and lower-right : *LMSA*.

Table 1 : Adopted Evolutionary Parameters

q_0	0.1	0.5
P	2.7	2.8
Q	1.4	1.5

Table 2 : Adopted Flux Limits of *IRIS* FIS

Wavelength [μm]	5σ -detection limit [mJy]
50	20
70	15
120	30
150	50

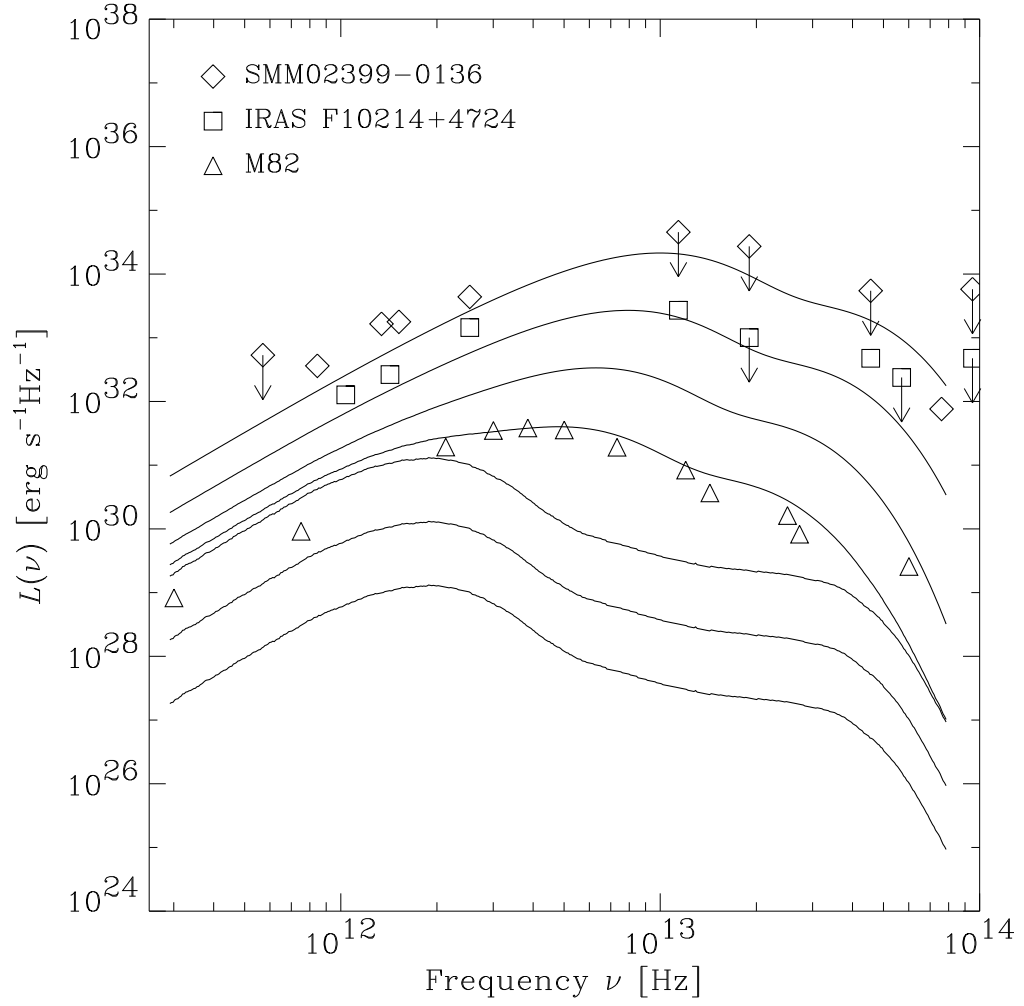


Figure 1

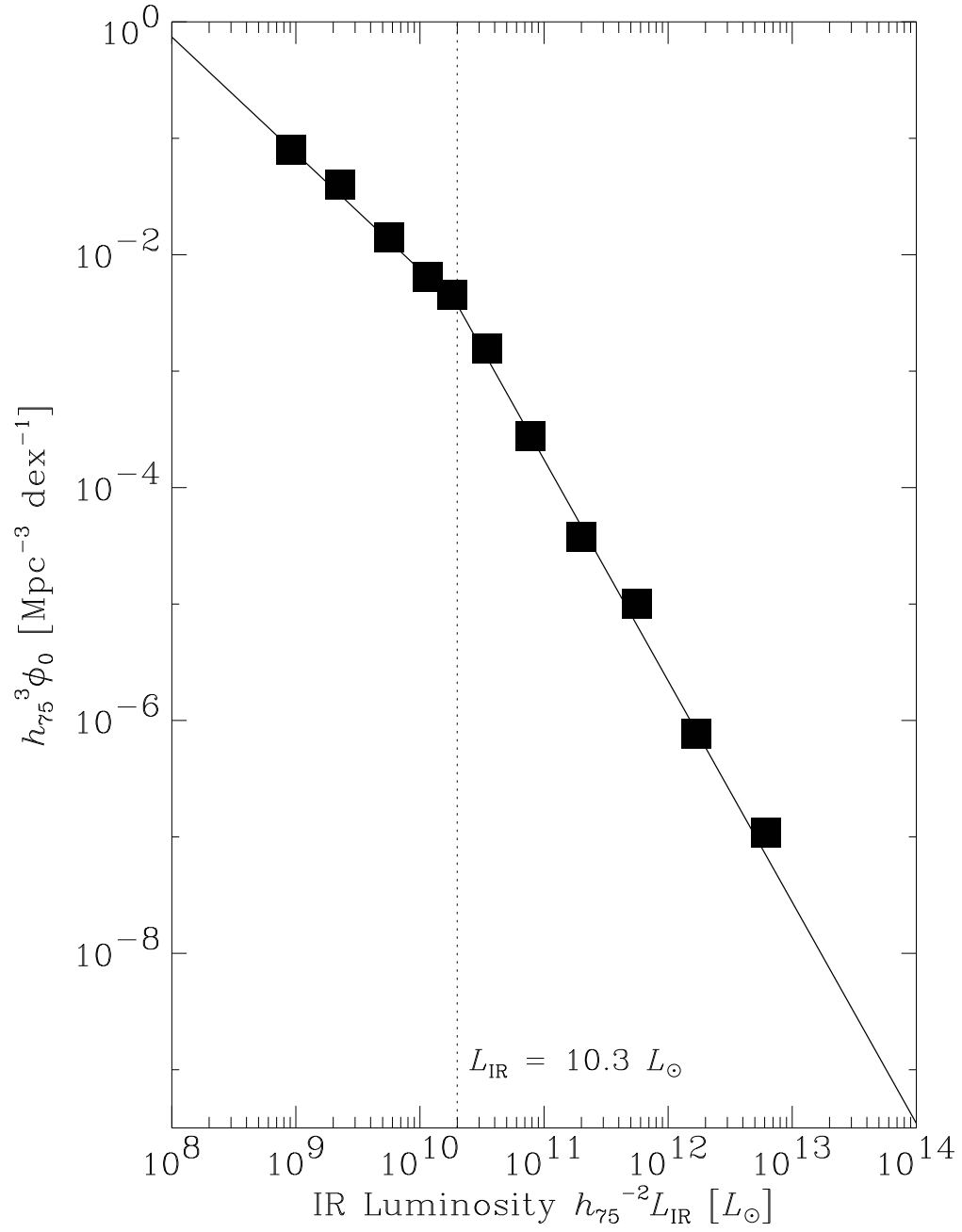


Figure 2

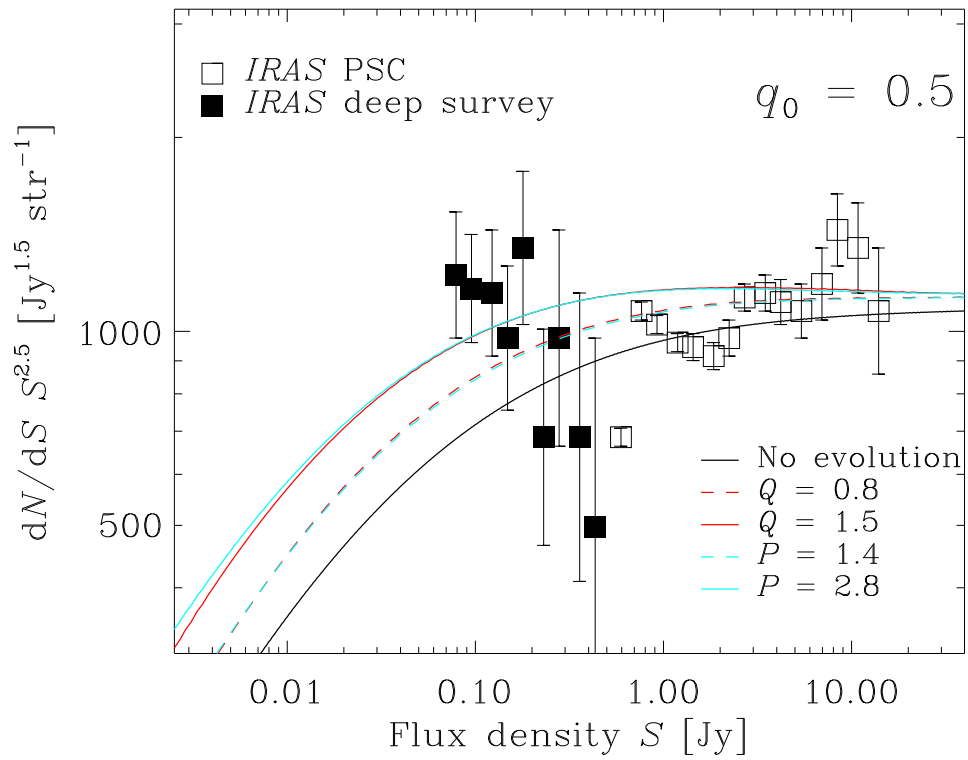
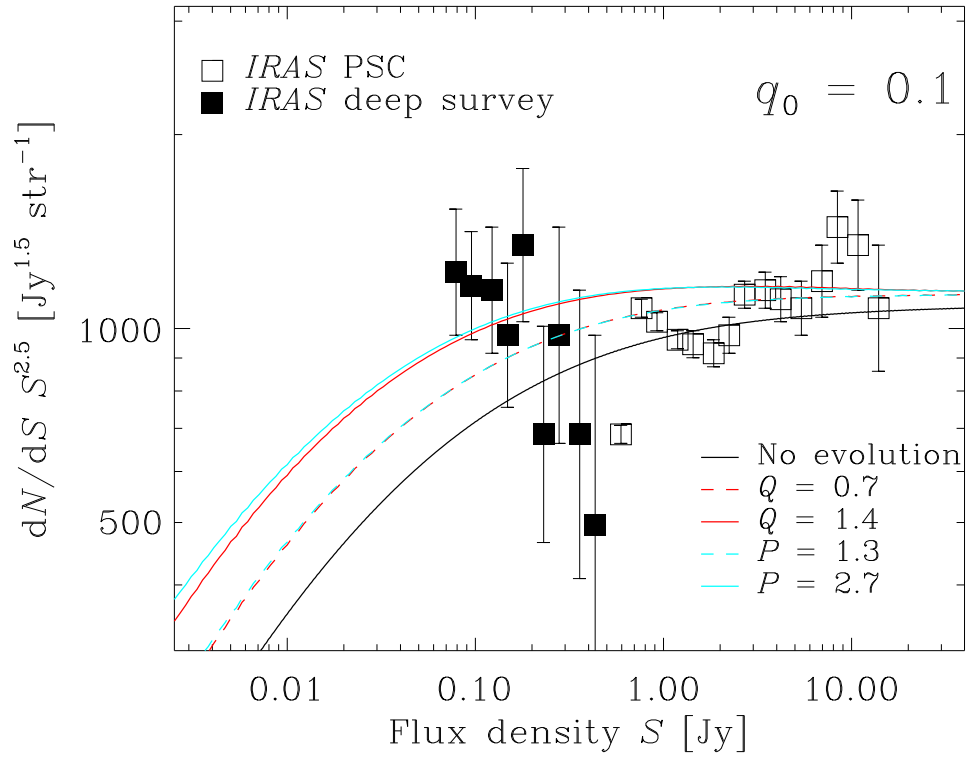


Figure 3

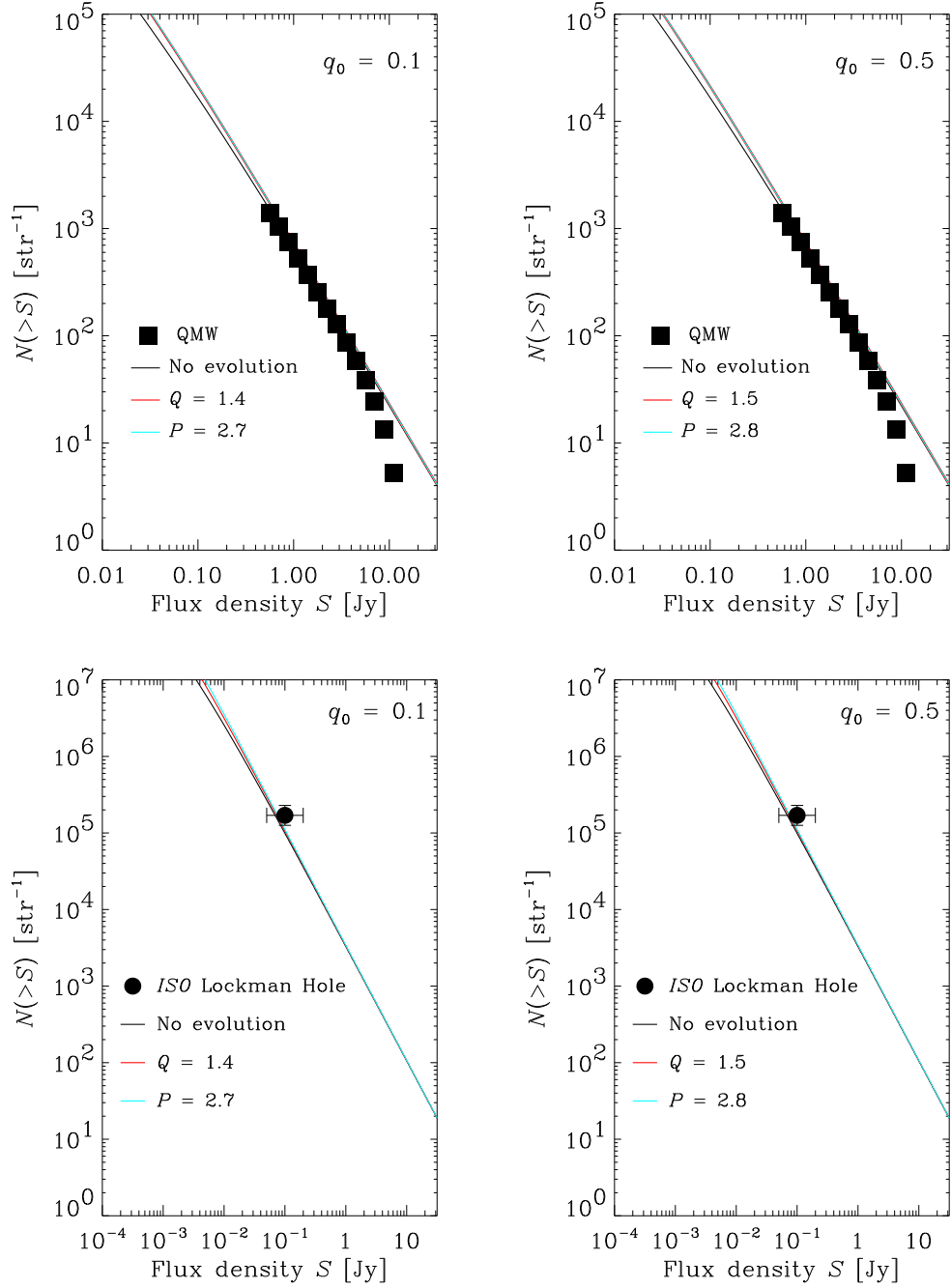


Figure 4

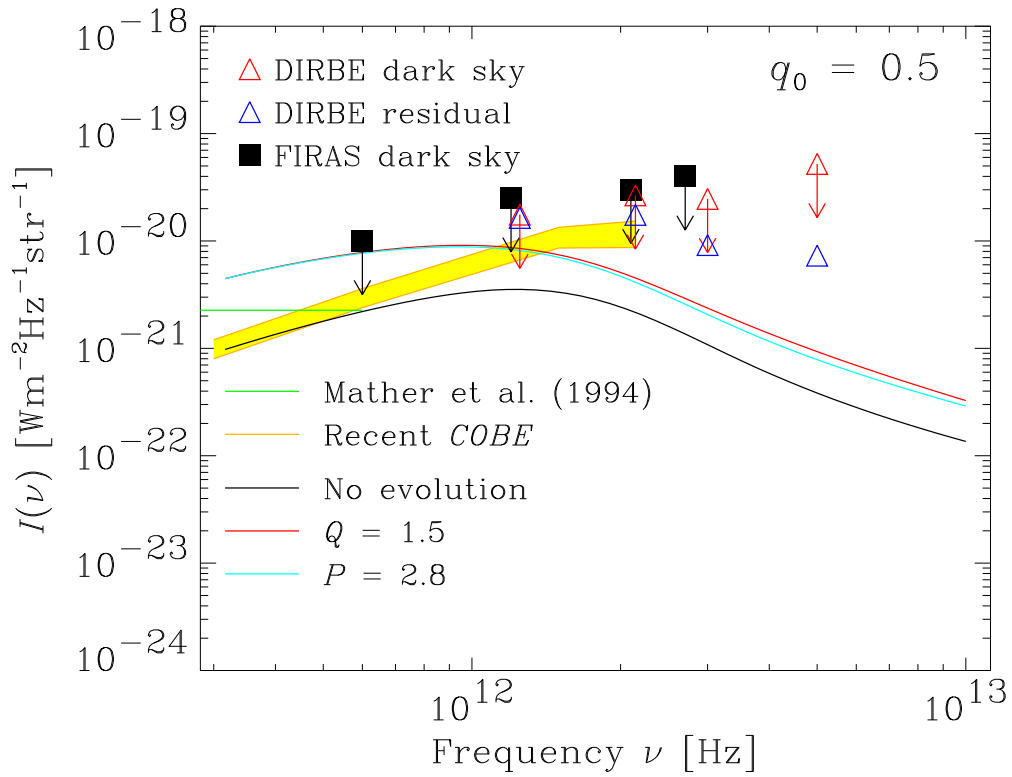
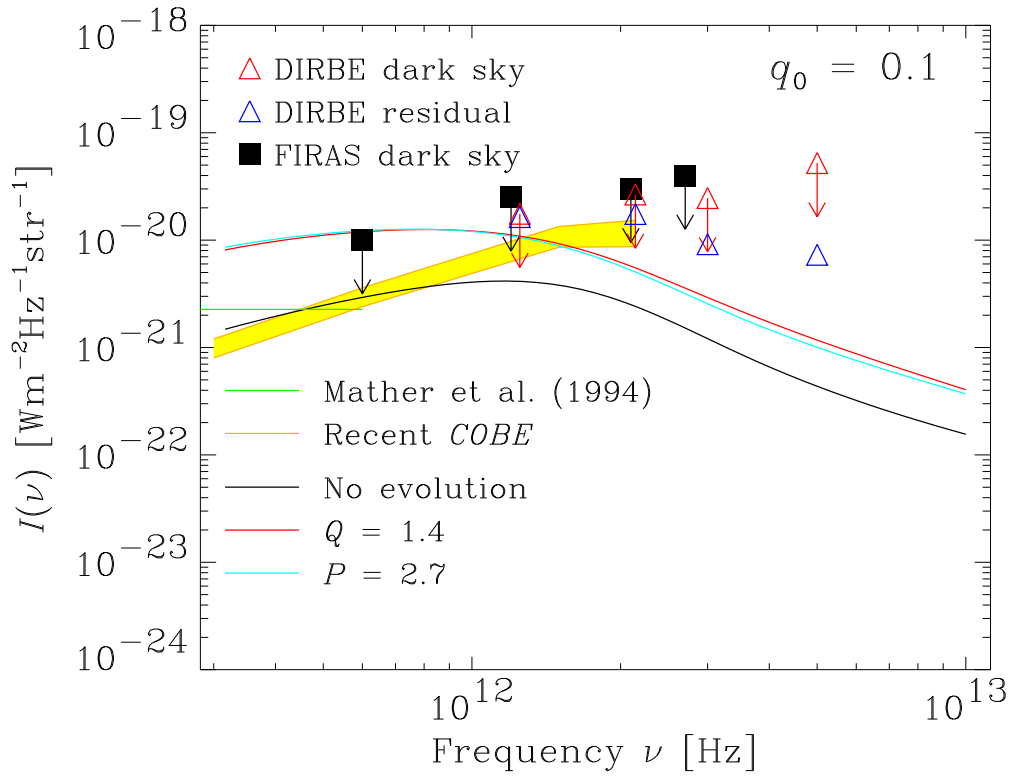


Figure 5

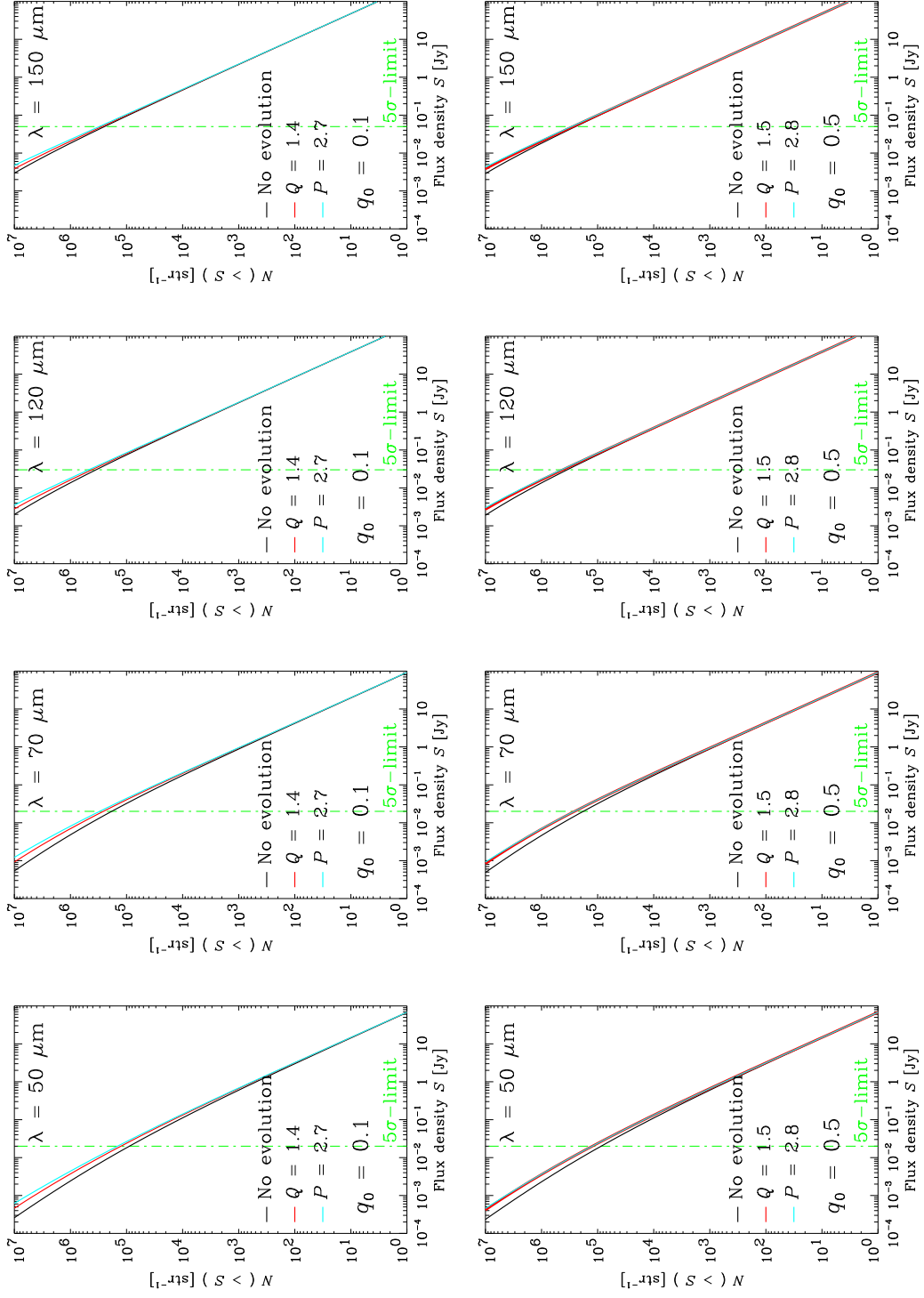


Figure 6

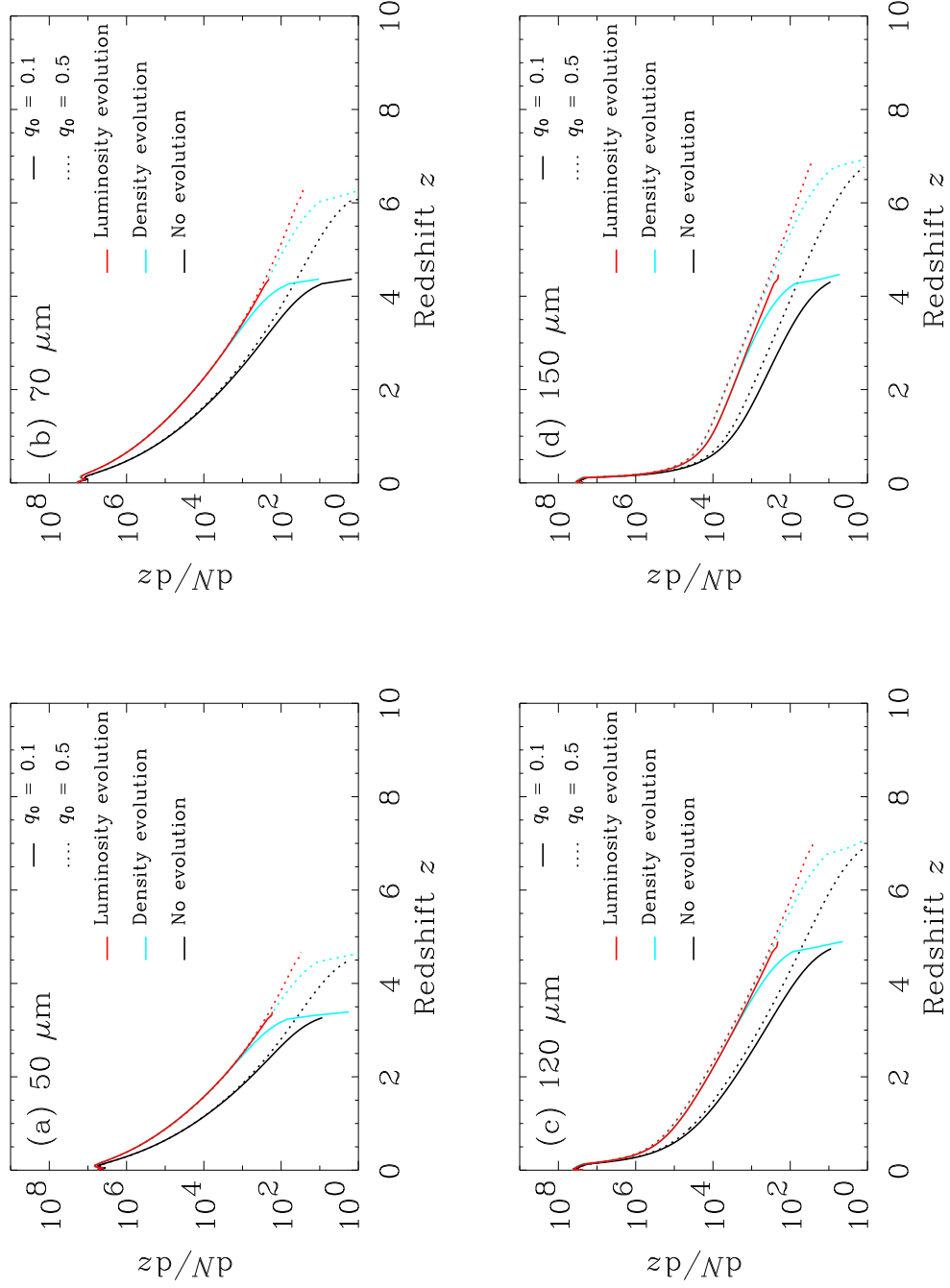


Figure 7

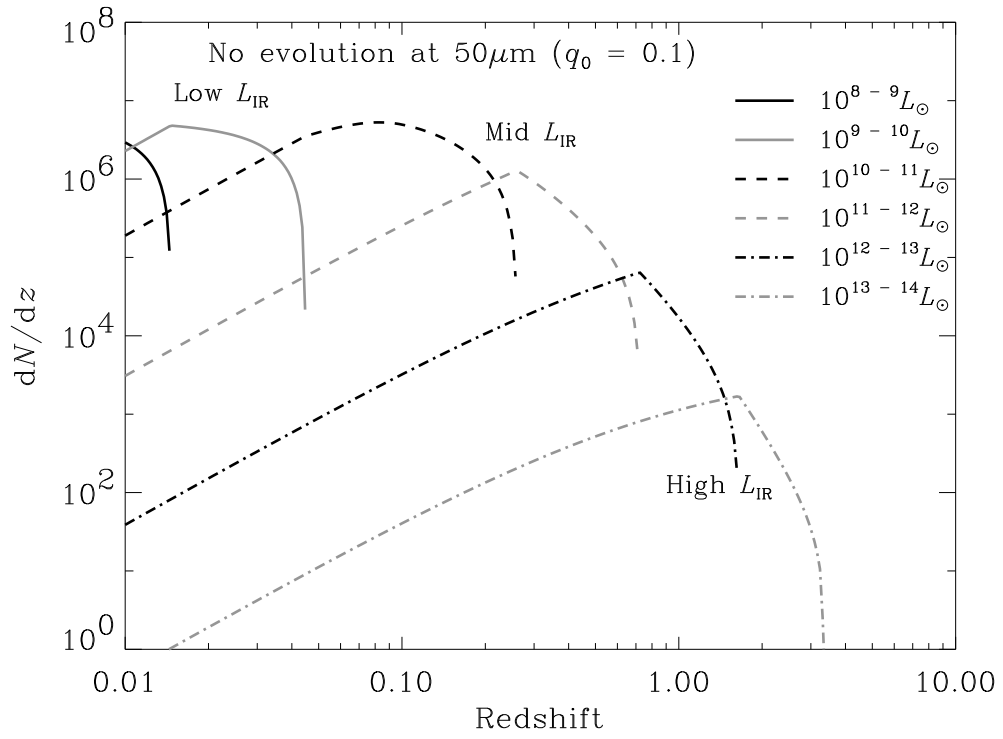


Figure 8

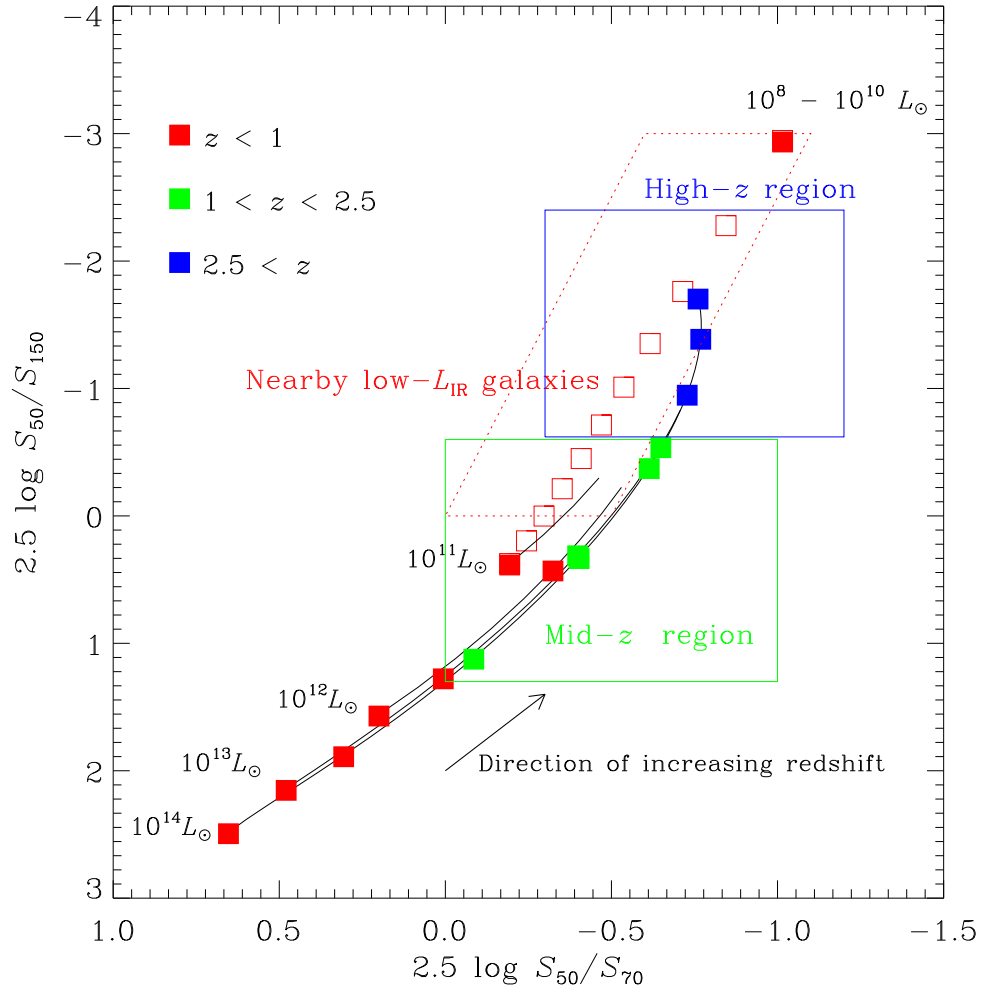


Figure 9

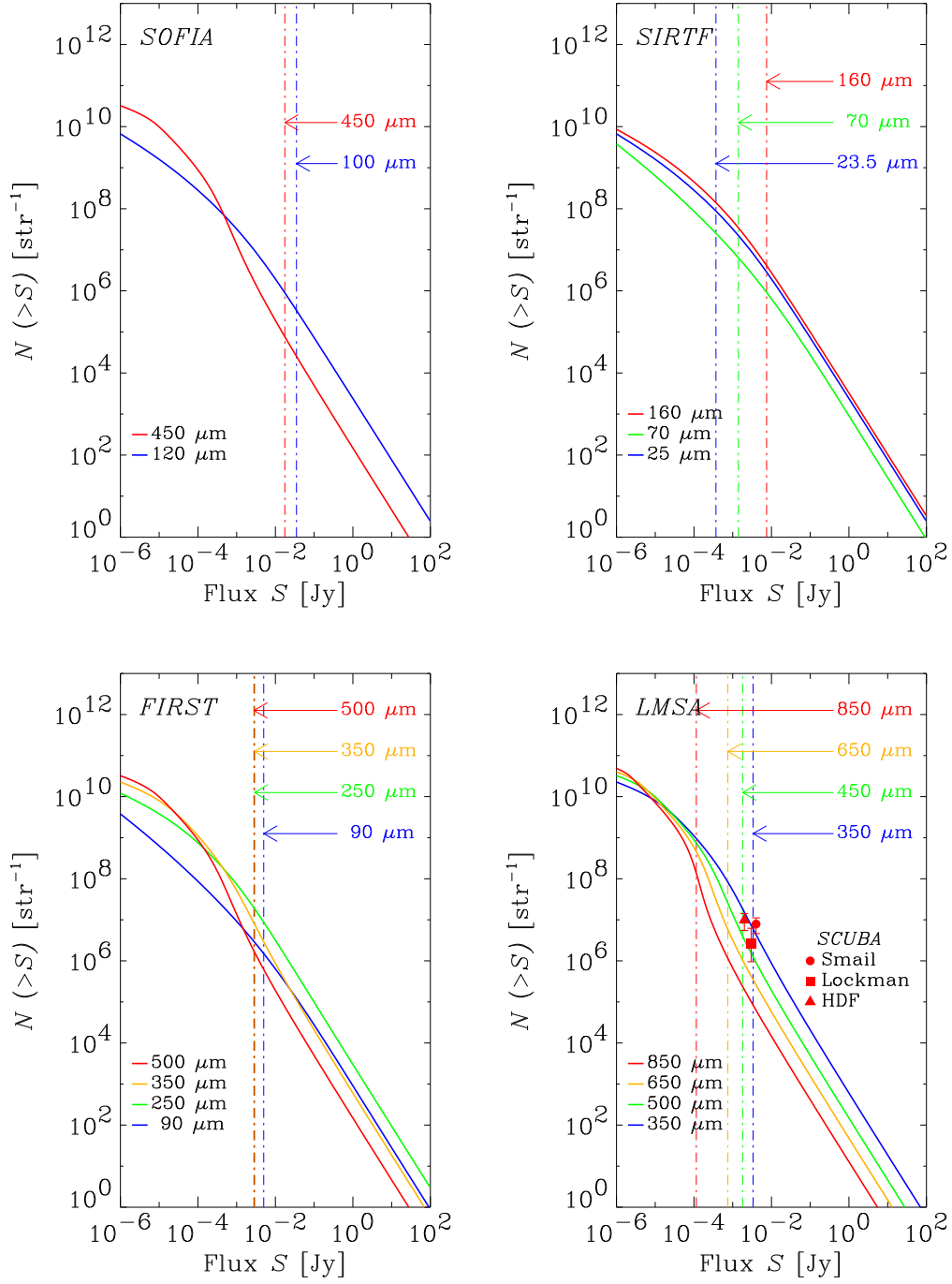


Figure 10

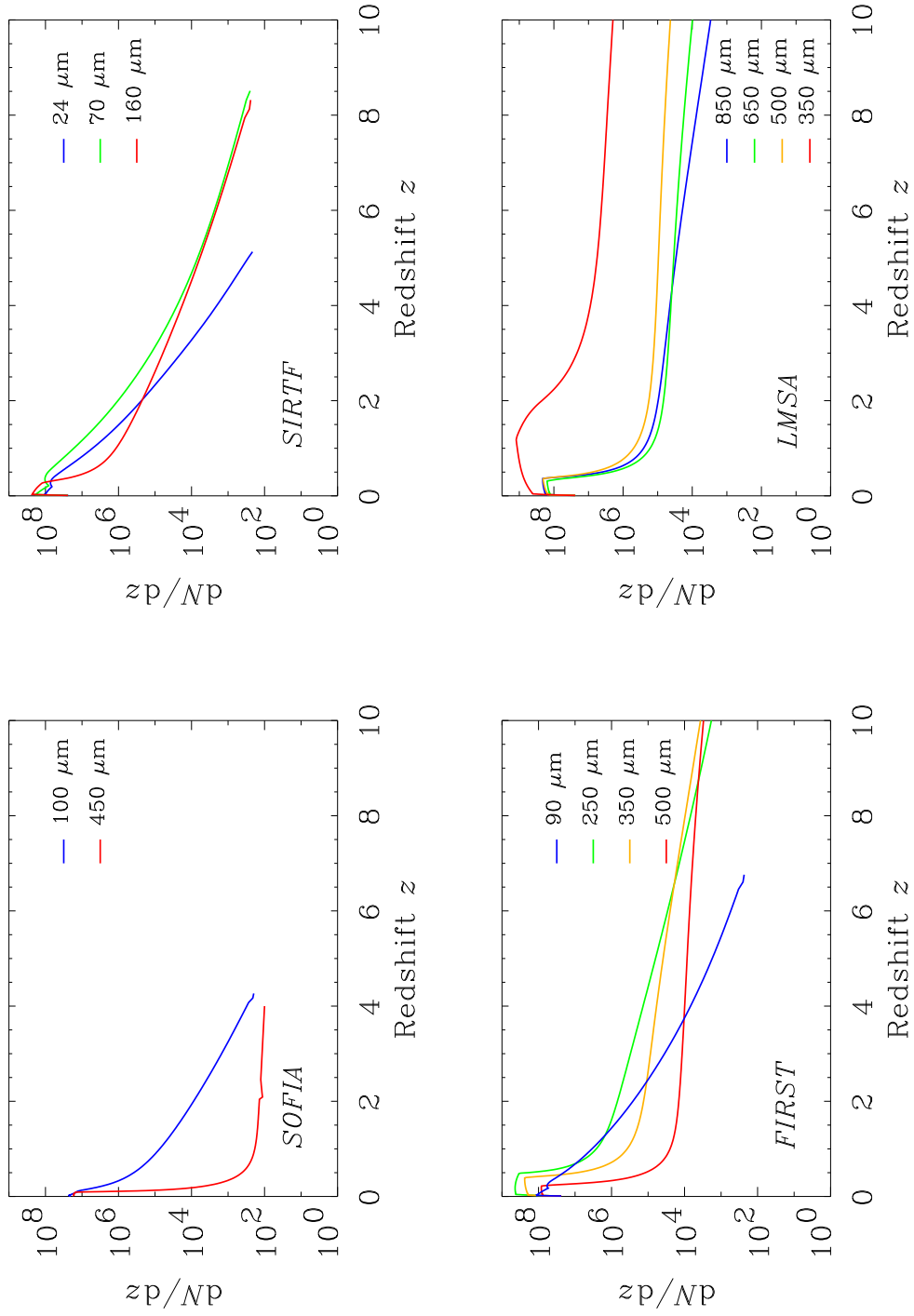


Figure 11